الجمهورية الجزائرية الديمقراطية الشعبية
République Algérienne Démocratique et Populaire
وزارة التعليم العالي و البحث العلمي
Ministère de l'enseignement supérieur et de la recherche scientifique

Université Mohamed Khider – Biskra

Faculté des Sciences et de la technologie

Département : Génie électrique

Ref :……

جامعة محمد خيضر بسكرة
كلية العلوم و التكنولوجيا
قسم: الهندسة الكهربائية
المرجع:……

Thèse présentée en vue de l'obtention
Du diplôme de

Doctorat 3ème cycle LMD en: Génie Electrique

Option: Signaux et Communications

Detection of Active Contour of Different Images (Détection du Contour Actif de Différentes Images)

Présenté par :

AZIZI Abdallah

Soutenue publiquement le 16 Octobre 2017

Devant le jury composé de :

Pr. BENAKCHA Abdelhamid	**Professeur**	**Président**	**Université de Biskra**
Pr. ELKOURD Kaouther	**Professeur**	**Rapporteur**	**Université d'Alger I**
Dr. GUEZOULI Larbi	**Maitre de Conférences 'A'**	**Examinateur**	**Université de Batna2**
Dr. TOUMI Abida	**Maitre de Conférences 'A'**	**Examinatrice**	**Université de Biskra**

Acknowledgment

First of all I wish to express my sincere gratitude to my advisor, Mrs. ELKOURD Kaouther, Doctor of University Benyoucef Benkhadda Algiers1. I am highly indebted and appreciated her for giving me the chance to explore on my own, her advices in every line that I wrote and the valued guidance to recover when my steps faltered.

I would like to thank my jury members, namely Mr. BENAKCHA Abdelhamid, Professor of University Mohammed Khider Biskra, Mrs. TOUMI Abida Doctor of University Mohammed Khider Biskra and Mr. GUEZOULI Larbi, Doctor of University Moustfa Benboulaid Batna2. Their time and energy are gratefully acknowledged. I want to appreciate very much for their detailed reviews and insightful comments. Special thanks to Dr. GUEZOULI Larbi for accepting to review this work and travelling to Biskra in order to serve on my committee.

Moreover, I would especially like to thank all the Electrical Engineering department staff, for their professional treatment of me as a colleague. Special thanks to post-graduation service, in particular Mrs. Akila.

I want to thank a number of researchers who helped me in this work in some way or another. Dr. KARABAGLI Bilal, Dr. FOI Alessandro, Dr. MANDAVA Ajay Kumar, Prof. REGENTOVA E Emma, Dr. TEUTSCH Michael, Dr. SCHUBERT David and the computer vision group at the technical university of Munich heading by Prof. CREMERS Daniel.

Last but not least, I would thank my family for their patience and encouragement during my study.

Abstract

Image segmentation is the problem of partitioning an image into different sub-regions based on a preferred feature. Segmentation is an important research area in image processing and plays a significant role in computer vision and object detection. A large number of different approaches have been developed to deal with segmentation problem including the active contour models (ACMs). The fundamental idea is to evolve an initial curve under some constraints from a given image to detect object boundaries by minimizing energy. Within this framework, this thesis aims at developing models dealing with problems of detecting objects (segmenting images) characterized by intensity inhomogeneity and noisy and poorly defined boundaries. To deal with these challenges, we proposed a number of ACMs relying on the level set method. The first one combines edge and region information based on an adaptive weighting function. The second approach uses local region-based signed pressure force in a simple and efficient level set formulation. Finally, the third one implements an edge-based segmentation with a novel stopping function based on local binary pattern (LBP). Experimental results demonstrate the high accuracy of segmentation obtained on various synthetic and real gray value images compared with state of the art ACMs.

Keywords: Active contour model, edge stopping function, Object detection, image segmentation, level set method, local binary pattern, region information, signed pressure force.

Résumé

La segmentation d'image est le problème de partitionnement d'une image en différentes sous-régions sur la base d'une caractéristique préférée. La segmentation est un domaine de recherche important dans le traitement d'images et joue un rôle important dans la vision par ordinateur et la détection d'objets. Un grand nombre d'approches différentes ont été développées pour traiter le problème de segmentation, y compris les modèles de contour actif (MCA). L'idée fondamentale est d'élaborer une courbe initiale sous certaines contraintes d'une image donnée pour détecter les limites d'objet en minimisant une énergie. Dans ce cadre, cette thèse vise à développer des modèles traitant de problèmes de détection d'objets (segmentation d'images) caractérisés par inhomogénéité d'intensité et des limites bruyantes et mal définies. Pour faire face à ces défis, nous avons proposé un certain nombre de MCAs s'appuyant sur la méthode d'ensemble de niveaux. Le premier combine les informations de contour et de région sur la base d'une fonction de pondération adaptative. La deuxième approche utilise la force de pression signée locale basée-région dans une formulation d'ensemble de niveaux simple et efficace. Enfin, le troisième implémente une segmentation basée contour avec une nouvelle fonction d'arrêt basée sur le motif binaire local (LBP). Les résultats expérimentaux démontrent la grande précision de la segmentation obtenue sur diverses images en niveaux de gris synthétiques et réelles par rapport à l'état de l'art des MCAs.

Mots-clés: Modèle de contour actif, fonction d'arrêt de contour, détection d'objet, segmentation d'image, méthode d'ensemble de niveaux, motif binaire local, information de région, force de pression signée.

ملخص

تقسيم الصور هي مشكل تجزئة الصورة إلى مناطق فرعية مختلفة بناء على ميزة معينة .التجزئة هو مجال بحث مهم في معالجة الصور ويلعب دورا هاما في الرؤية بالكمبيوتر والكشف عن الأجسام . وقد تم تطوير عدد كبير من المناهج المختلفة للتعامل مع مشكلة التجزئة بما في ذلك نماذج الحيز النشطة . الفكرة الأساسية هي أن يطور حيز أولي تحت بعض القيود من صورة معينة للكشف عن حدود الجسم عن طريق التقليل من الطاقة .في هذا الإطار، تهدف هذه الأطروحة إلى تطوير نماذج للتعامل مع مشاكل الكشف عن الأجسام (بتجزئة الصورة) التي تتميز بعدم تجانس الشدة، والحدود المشوشة وغير المحددة بشكل واضح .للتعامل مع هذه التحديات، اقترحنا عددا من نماذج الحيز النشطة اعتمادا على طريقة مجموعة المستويات .أولها يجمع بين معلومتي الحافة والمنطقة بالاعتماد على دالة مكيفة للترجيح. النموذج الثاني يستخدم قوة ضغط مؤشرة مبنية على معلومة المنطقة المحلية في معادلة مجموعة مستويات بسيطة وفعالة . وأخيرا، النموذج الثالث مبني على تجزئة تعتمد على معلومة الحافة مع دالة توقف جديدة تقوم على النمط الثنائي المحلي (LBP) .تظهر النتائج التجريبية دقة عالية للتجزئة المحصل عليها على صور رمادية مختلفة اصطناعية وحقيقية مقارنة مع أمثلة الحيز النشطة المعروفة.

الكلمات المفتاحية: نموذج الحيز النشط، دالة التوقف بالحافة، كشف الأجسام، تجزئة الصورة، طريقة مجموعة المستويات، النمط الثنائي المحلي، معلومات المنطقة، قوة الضغط المؤشرة.

Publications

The research outcomes of this thesis are reported in the following publications:

Journal Papers:

- Azizi, A., & Elkourd, K. (2016). Fast Region-based Active Contour Model Driven by Local Signed Pressure Force. *ELCVIA Electronic Letters on Computer Vision and Image Analysis*, *15*(1), 1-13.

- Azizi, A., Elkourd, K., & Azizi, Z. (2017). Robust Active Contour Model Guided by Local Binary Pattern Stopping Function. *Cybernetics and Information Technologies*, under review.

Conference Papers:

- Abdallah, A., & Kaouther, E. (2015, November). A Hybrid Active Contour without Re-initialization. In *Proceedings of the International Conference on Intelligent Information Processing, Security and Advanced Communication* (p. 45). ACM.

Abbreviations

ACM: **A**ctive **C**ontour **M**odel.

C-V: **C**han-**V**ese.

DRLSE: **D**istance **R**egularized **L**evel **S**et **E**volution.

ESF: **E**dge **S**topping **F**unction.

GAC: **G**eodesic **A**ctive **C**ontour.

GACV: **G**eodesic **A**ided **C**han **V**ese.

LBF: **L**ocal **B**inary **F**itting.

LBP: **L**ocal **B**inary **P**attern.

LBPSF: **L**ocal **B**inary **P**attern **S**topping **F**unction.

LGDF: **L**ocal **G**aussian **D**istribution **F**itting.

LSE: **L**evel **S**et **E**volution.

LSF: **L**evel **S**et **F**unction.

LSM: **L**evel **S**et **M**ethod.

LSPF: **L**ocal **S**igned **P**ressure **F**orce.

M-S: **M**umford-**S**hah.

ORACM: **O**nline **R**egion-based **A**ctive **C**ontour **M**odel.

PDE: **P**artial **D**ifferential **E**quation.

SBGFRLS: **S**elective **B**inary and **G**aussian **F**iltering **R**egularized **L**evel **S**et.

SDF: **S**igned **D**istance **F**unction.

SPF: **S**igned **P**ressure **F**orce.

Contents

List of figures

List of tables

Introduction

1.1. Image segmentation

Image segmentation is the most studied problem in computer vision. We will start with an example showed in Fig. 1.1 demonstrates that the segmentation is a difficult problem even for humans; typically we are in stage today where things that are easy for humans are difficult for computers. Refers to Fig. 1.1, not many humans recognize what's on the image; it is a Dalmatian dog (white dog with black spots), this problem of detecting and separating objects from background is called segmentation. More specifically image segmentation can be formally described as:

Definition1.1.

Let Ω *be an image domain. Image segmentation refers to the process of partitioning* Ω *into disjoint sub-regions* $\{\Omega_r\}, r = 1, \dots, N,$ *which satisfy* [1] :

1. $U_{r=1}^{N} \Omega_r = \Omega;$
2. $\Omega_a \cap \Omega_b = \emptyset, \forall a \neq b;$
3. $P(\Omega_r) = true, \forall r;$
4. $P(\Omega_a \cap \Omega_b) = false, \forall a \neq b.$

P(.) is a logical predicate defined on groups of connected pixels.

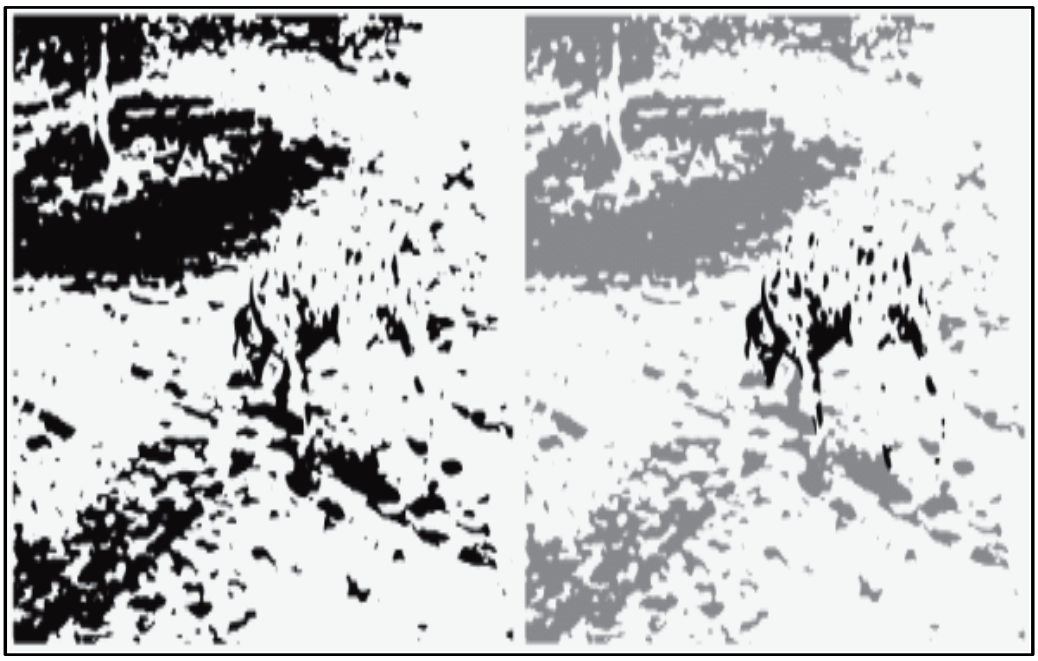

Figure 1.1: Binarized image of a Dalmatian dog in a background of leaves (left). The dog is located to the right of the center with its back to the viewer (right) [2].

There exist many approaches to tackle segmentation problem, they typically differ in the following ways:

- Which local properties are considered to compute segmentation (brightness, color, texture, motion...).
- How the segmentation is computed; once the criterion which the segmentation is based on is decided, the next question is what's the algorithm used to group pixels (region merging, region growing, level sets…).

  Segmentation methods are generally classified into five categories [3]:

1.1.1 Thresholding segmentation

Thresholding methods are pixel based strategies, and usually convert an image into a binary image containing two subsets (foreground and background) based on a threshold value (θ). The idea is to label each pixel as one "1" (object) if its brightness is larger than the threshold value (θ) or zero "0" (background) if it is darker than (θ).

The challenge in these methods is to find a good threshold value. There are a lot of strategies doing that including Otsu's thresholding [4] which is the most popular. This method proposed a particular threshold such that the brightness variance of the object and background are minimized; the algorithm tries to find brightness threshold between object and background in such a way that the pixels that form the object have minimum variance of brightness and similarly for the background. Thresholding has many advantages; typically is very fast and it can be run in real time.

In addition it has adaptive variants that can improve the performance (brightness distribution and brightness variance). However thresholding neglect spatial context (i.e the information that neighboring pixels are likely to be part of the same region. Instead all pixels are treated independently).

1.1.2 Clustering methods

They are systematic approaches to tackle thresholding; the idea behind clustering is to compute segmentation of an image by combining pixels of similar brightness in a single region (cluster) and representing theses clusters by probabilistic distribution. There are many clustering algorithms and the most common one is K-means clustering [5]. This method determines a given number of K clusters by iteratively assigning data points to the nearest of K cluster center and subsequently re-computing these cluster centers to represent the segmented image, each data point is replacing with the cluster center of that cluster. In principle, this method is a form of segmentation because all pixels are partitioned into groups, but it is actually a little more what is called "brightness quantization"; by getting a good approximation of the original image with just K levels and this could be used for example for image compression.

1.1.3 Edge-based segmentation

This method identify contours which approximate discontinuities of the gray level, color, texture….The location of discontinuities is given by an extreme of either the first order derivative of the image intensity [6,7] or the zero crossings of second order derivative [8], one of the most accurate techniques in this category is the Canny edge detector [9]. The canny edge detector is less sensitive to noise than other first derivative edge detector; taking image derivatives leads to accentuate high frequencies as noise and the canny algorithm convolves the image with a Gaussian filter (low pass filter) to smooth it. Although these methods are easy to be implemented, they are very sensitive to noise and they are likely to produce gaps between boundaries [10].

1.1.4 Region-based segmentation

This category is in some sense complementary to the previous category; that it identifies regions in the images plane for which some criterion is more or less uniform (brightness, color, texture…). Two rather old methods for computing region-based segmentations are region merging and region growing [11,12]. Both methods are similar in their principle but they go slightly different ways; the idea is to find segmentations by aggregating pixels into regions. In region growing, one start with a couple of seed pixels and then iteratively include neighboring pixels (grow regions) as long as their predefined criterion is sufficiently similar. Region merging approach starts with a partitioning for which each pixel is its own region and then, iteratively merges (fusion) neighboring regions as long as they are sufficiently similar. The advantage of these techniques is that they are interactive in some way and they always determine connected regions, but they typically lack a systematic optimization criterion.

1.1.5 Energy-based segmentation

These methods form the segmentation problem as an optimization problem which tries to divide the images into regions by optimizing some criterion (minimizing or maximizing energy) [13].

Active Contour Models (ACMs) [14] are the most popular techniques in this category; the idea behind the ACM is to drive an initial curve inside the image domain to be segmented to reach the boundaries of the objects of interest by minimizing energy. Where the curve is argument of this energy [15], one of the questions that we will look for: how does the boundary is represented? According to curve representation there are two types of ACMs, parametric models and geometric models. Parametric ACMs [16-18] are implemented explicitly as parameterized curves with a set of control points, and evolving the curve is reached by evolving these control points. However, by construction, parametric curves have a fixed topology; without additional splitting or merging heuristics, the curve topology will not change during its evolution. Geometric ACM are independently introduced by Casselles *et al* [19,20] and Malladi *et al* [21]. These models combining curve evolution theory [25] and level set method (LSM) [26], give sophisticated solution to overcome the limitation of parametric ACM. The key idea is to evolve a level set function (LSF) where the curve is representing its zero level. The main advantage of this approach is that the topological changes of the curve represented by the LSF are handled automatically.

According to the LSM strategy, there are two different strategies to tackle segmentation with LSM: partial differential equation (PDE) based ones [19-22] and variational ones [23,24]. The level set evolution (LSE) of PDE based LSM is directly derived by implementing the gradient descent equation for the curve using the level set equation. This was done to derive the LSM for snake-like energies known as geodesic active contour (GAC) [20,22]. The LSE of variational LSM is derived by rewriting the variational principle with respect to the LSF rather than the curve, and then computing the gradient descent with respect to this function [23,24]. This method presents advantages over PDE based one, that it is more robust and more convenient for incorporating additional information such as shape and region location [27].

The energy has two components, one is the regularity term or internal energy and one is the data term or the external energy. The internal energy is a regularizer which induces some smoothness on the curve. External energy is image-driven; that is based on different image characteristics. According to image characteristics ACM can be classified into two main categories: edge-based models and region-based models. Edge-based models [20,23] rely on local image gradient information to construct an edge stopping function (ESF) to stop the evolving curve on the desired objects boundaries. Although these models have been successfully applied for images with height variation in gradient at objects boundaries even in the presence of intensity inhomogeneity, they meet difficulty when dealing with object having blurred or discrete boundaries and they hardly detect objects corrupted by noise [28]. Region-based models form the foreground and background regions statistically and find an energy optimum where the model best fits the image [29]. These models control the evolution of the

curve with better performance including weak edge and noise. However, modelling regions using global statistics [24,30] is not applicable to images with intensity inhomogeneity. Although, some region-based models using local statistics have been proposed to deal with intensity inhomogeneity [31-33] but they are found to act locally, to be easy to trap into local minima and the local statistics are only defined empirically, which make these models sensitive to the choice of those statistics [34].

1.2. Motivation

Current ACMs, either edge-based models or region-based models (using global or local statistics) are efficient to some extent to handle segmentation problem. However, they have shortcomings when dealing with noisy images for edge-based ACMs, or with images have several intensity levels or with intensity inhomogeneity for region based-models even with the use of the local statistics; such models are found to be less robust to noise and very time consuming.

As a consequence, these problems need to be addressed, such as:

- Can edge and region information be combined in a single model?
- Is it possible to develop a local region-based model which is computationally efficient and robust to noise?
- Can edge based models be ameliorated to deal with noise but keeping sophisticated edge structures?

Motivated by these issues, we mainly focus on:

- Combining edge and region information in a variational level set formulation.
- Develop fast and robust local model to deal with images characterized by many intensity level or intensity inhomogeneity by using a new level set formula and new regularizers.
- Construct a robust and effective edge-based model based on a new approach which is a crossover between edge detection and texture analysis.

In this work, we will focus on the two regions case (object/background) with only gray level images.

1.3. Organization of the dissertation

In this thesis, we focus on studying segmentation methods for images with noisy or poorly defined objects boundaries and with intensity inhomogeneity or with several intensity levels. For that, we begin by the review of the main concepts of the ACMs and the different types. We will then discuss the weaknesses met with each type. Finally we will propose possible solutions to address these problems.

The remainder of this thesis is organized as follow:

- In chapter 2, we review the state of art of ACMs and the different types based on the curve representation, the LSM strategy and the information used, we will focus on their strength and weaknesses.
- Chapter 3 presents the proposed hybrid edge and region based ACM in a variational level set formulation; by combining both edge and region information, the energy functional of the proposed level set formulation is defined with a region term, which allows bidirectional motion of the curve and drives it when it is far away from object boundaries, and an auxiliary edge term which attracts the curve and stop it at objects boundaries. In addition, a regularization term is added to the energy functional to ensure accurate computation and avoid expensive re-initialization of the evolving LSF.
- In chapter 4, we propose within a PDE level set formalism an ACM based on local image region statistics. The proposed model has the following strength: it can handle intensity inhomogeneity problem by introducing a new region based signed pressure force (SPF) function which uses the local region means values inside and outside the curve to guide the curve evolution; it offers high efficiency and rapid convergence by using a simple and efficient level set formula which uses directly current LSF instead of its curvature approximation, and it is robust to some extent to noise by using a new regularizer such as morphological opening and closing operations to remove small objects and smooth the curve.
- Chapter 5 describes our proposed ACM based on the Local Binary Pattern (LBP). The gradient stopping function that is widely used in edge-based ACM as an edge indicator is high sensitive noise and poorly defined boundaries. Inspired by recent development for edge detection, we use LBP textons to construct an LBP stopping function (LBPSF). The classification of image regions by LBP textons into noisy, homogeneous regions, and edges helps to generate a filter rejecting pixel positions of noise and detect edges using a modified Canny edge detector in such a way, the new stopping function takes the value of "0" on edge to stop the motion of the curve while has value of "1" on noisy and homogeneous regions.
- Finally the last chapter concludes the present work and presents a number of limitations of the proposed methods and some possible future work directions.

Active contour models

2.1. Introduction

Classical image segmentation methods lack a mathematically or rigueur transparent optimization criterion. This is where energy-based segmentation enters the picture. The key idea is to define cost functionals over a solution space and to compute optima by solving the corresponding extremality principle. This method allows solving segmentation problem in a mathematically transparent manner. Instead of performing a heuristic sequence of processing steps, one starts by defining what properties a solution should have. The most popular technique in this method are ACMs; The main idea is to segment an object by iteratively deforming (evolving) a given initial curve until it reaches the edges of the object by minimizing energy calculated from different criteria. During the minimizing process, the points of the curve will move so that the curve at the following iteration has a lower energy, and the curve evolves until it reaches the border of the desired object [35].

To build an ACM, there are mainly three criterions that we based on; the curve representation, the level set strategy used and the information or image characteristics used. This chapter reviews the main types into each category, its theoretical framework, advantages and weaknesses.

The goal of this chapter is to give an introduction to the theory behind ACMs, their similarities, differences and problems to motivate the proposed methods those will solve some of these problems later on.

The outline of this chapter is as follow: we start with describing two well-known categories of ACMs based on image characteristics. Namely snakes (edge-based method) and the Mumford-Shah (M-S) functional (region-based method).

This helps us to study other categories based on the curve representation (parametric and geometric), the level set strategy (PDE and variational) which is the content of the next section. The last section focuses on using local regions statistics to build local region-based ACMs that will be presented and discussed.

2.2. Snakes

The snake model proposed by Kass *et al* [14] in the late 80th, to our knowledge, is the first ACM. The idea is to minimize an energy given by:

$$E(C) = \int \{\frac{\alpha}{2}|C_s|^2 + \frac{\beta}{2}|C_{ss}|^2 - |\nabla I(C)|^2\} ds \qquad (2.1)$$

Here C denotes an explicit parametric curve, C_s and C_{ss} denote the first and the second derivative with respect to the curve parameter. The first two terms of (2.1) weighted by α and β are the regularity term or the internal energy of the contour, measuring the length and the stiffness of the contour.

The last term is the data term or external energy which accounts for image information, in the sense that the minimizing contour will favor locations of large image gradient [2], minimizing the total energy leads to curves which are short and stiff while passing through locations of large gradient. Minimizing of (2.1) by gradient descent results in the following evolution equation[1]:

$$\frac{dC(s,t)}{dt} = -\frac{dE}{dC} = \alpha C_{ss} - \beta C_{ssss} + \nabla|\nabla I(C)|^2 \tag{2.2}$$

The snake is among the most influential publications in image processing and is considered as the first variational approach to image segmentation[2]. However, it still has several limitations:

- The initial curve must therefore be initialized sufficiently close to the desired solution because the external energy is active only close to object boundary. Alternatively one can presmooth the input image (to propagate gradient information). Yet, the smoothing also removes possibly important edge information (Fig. 2.1). Several methods have been proposed to address problem of initialization of the curve [17-18,36-38] in aim of propagating the edge information into the image to increase the capture range of external energy.
- The evolution of parametric curves is a challenging problem as one needs to avoid self intersections. More details about this problem are given in section 2.4.

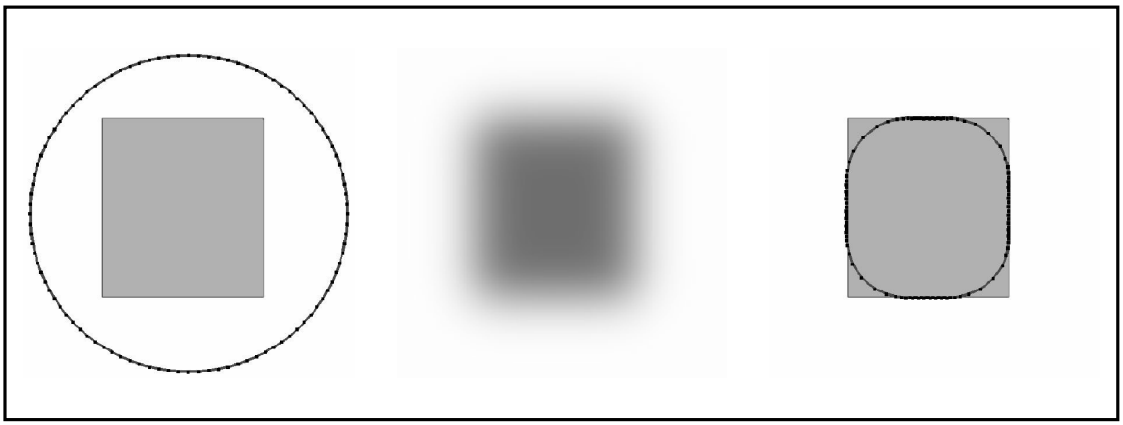

Figure 2.1: Segmentation example using snake model [14]. From left to right: input image with the initial contour, Gaussian-smoothed input image, the final segmentation (implementation: D. Cremers).

[1] The theory behind functional minimization is developed in Appendix A.

[2] To Dec'16, it has acquired more than 19000 citations.

2.3. The Mumford-Shah model

The M-S model [39] was proposed to compute segmentation integrated with image de-noising. It searches for a piecewise smooth approximation by minimizing the functional:

$$E(u,C) = \frac{1}{2}\int_{\Omega}(I-u)^2dx + \frac{\lambda}{2}\int_{\Omega-C}|\nabla u|^2dx + \upsilon|C| \tag{2.3}$$

Simultaneously with respect to the image u and with respect to the curve C. the three terms have the following meaning:

- The data term (first term) assures that u is a faithful approximation of the input image I; it just that we want to compute an approximation u of the original image that matches the image in a least square sense.
- The smoothness term (second term) weighted by $\lambda > 0$, assures that u is smooth everywhere except for the boundary C.
- A further regularizer weighted by $\upsilon > 0$ assures that this boundary has minimal length $|C|$.

For increasing value of the weight λ, the approximation u is forced to be smoother and smoother outside of C. In the limit $\lambda \to \infty$, we obtain a piecewise constant approximation of the image I[3]:

$$E(u,c) = \int_{\Omega}(I(x)-u(x))^2dx + \upsilon|\mathrm{C}| \tag{2.4}$$

Where $u(x)$ is constant in each of the regions separated by the boundary C. If we denote these regions by $\{\Omega_1, \Omega_2 \dots \Omega_n\}$ and the constants u_i; this can be rewritten as:

$$E(\{u_1, u_2 \dots u_n\}, C) = \sum_{i=1}^{n}\int_{\Omega_i}(I(x)-u_i)^2dx + \upsilon|\mathrm{C}| \tag{2.5}$$

Minimizing of (2.5) results in an approximation of the input images I by a function u which is piecewise constant on a set of regions Ω_i separated by the boundary set C, where the constants u_i; are given by the average brightness in each region:

$$\frac{\partial E}{\partial u_i} = 2\int_{\Omega_i}(I(x)-u_i)^2dx = 0 \implies u_i = \frac{\int_{\Omega_i} I(x)dx}{\int_{\Omega_i} dx} \tag{2.6}$$

For the piecewise constant M-S functional, and only two regions separated by a curve C. Zhu and Yuille [40] proposed to minimize the piecewise constant M-S as[4]:

$$\frac{\partial C(s,t)}{\partial t} = -\frac{dE}{dC} = ((I-u_{ext})^2 - (I-u_{int})^2 - \upsilon K_c)\overrightarrow{n_c} \tag{2.7}$$

Where $\overrightarrow{n_c}$ is the outer normal and K_c denotes the local curvature of C.

If the local brightness $I(x)$ at a point x in the curve C is more similar to the average brightness of the interior, then x is assigned to the interior (the curve moves outward) and vice versa (Fig. 2.2). In addition the evolution aims at suppressing large curvature of the

[3] For $\lambda = 0$ we get the same cost function, but the constraint is $u = cste$, and with $\lambda = 0$, u can be equal to I and this solve the problem.

[4] The technical details of this implementation are described in Appendix B.

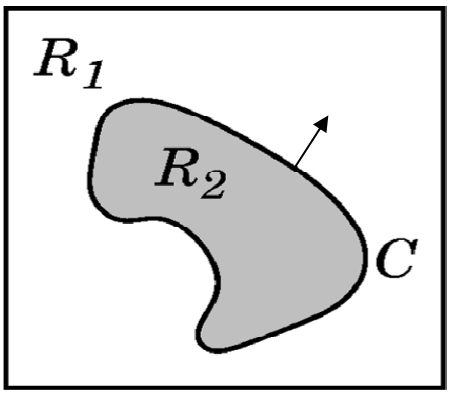

Figure 2.2: Competition between two adjacent regions; at each boundary point, displace the curve: outwards, if $|I - u_{int}| < |I - u_{ext}|$, inwards if $|I - u_{int}| > |I - u_{ext}|$.

curve; this is what leads to a local minimization of the boundary length $|C|$. Other implementation of the M-S functional within the level set framework has been proposed by Chan and Vese [24] and by Yezzi *et al* [41].

2.4. Level set methods

The level set methods have been extremely popular as a representation for evolving curves, and what we saw in the previous sections, one very straightforward way is to represent a curve as points of the boundary and that could be in the simplest case a polygon, and in a more sophisticated setting a spline; this is called a parametric representation of the boundary or explicit representation. The level set method is very different from that; it is what called an implicit representation.

2.4.1. Explicit VS implicit curve representation

Gradient descent on respective Functional $E(x)$ leads to an evolution of the boundary in normal direction, which can be implemented explicitly or implicitly. Explicit boundary evolution has the following strength (+) and weaknesses (-):

+ Explicit evolutions are runtime and memory efficient, allowing a fast evolution of highly detailed boundaries.
+ Prior shape knowledge can be imposed directly on the evolving boundary.
- The numerical propagation of explicit boundaries is prone to instabilities, as self-intersections have to be avoided and re-gridding of control points may be necessary.
- Respective functionals are typically not convex with respect to the boundary C. hence solutions are typically only locally optimal.

2.4.1.1. Explicit curve evolution

Gradient descent on a functional $E(x)$ leads to an evolution of the curve C:

$$\dot{C} = \frac{dC}{dt} = Fn \tag{2.8}$$

With some speed F in direction of the outer normal n. A parametric representation of the curve as a spline is given by:

$$C(s,t) = \sum_{j=1}^{n} x_j(t) B_j(s) \tag{2.9}$$

With control points $x_1, x_2 \ldots x_n \in \Re^2$ and basis functions $B_1, \ldots B_n$ (Fig. 2.3). Inserting the spline representation into the evolution equation gives:

$$\dot{C} = \sum \dot{x}_j(t) B_j(s) = Fn \tag{2.10}$$

Projection into the basis function B_K leads to:

$$< B_k, \dot{C} >= \sum_j \dot{x}_j(t) < B_k, B_j >=< B_k, F_n >= \int B_k(s)\, F(s) n(s) ds \tag{2.11}$$

This is a linear equation system in X_j, namely:

$$B\dot{x} = q \text{ with } B_{kj} =< B_k, B_j > \text{ and } q_k =< B_k, F_n > \tag{2.12}$$

The temporal evolution of control points is given by:

$$\dot{x} = B^{-1} q \tag{2.13}$$

Time discretization leads to an update of the control points x:

$$x(t+\tau) = x(t) + \tau \dot{x}(t) = x(t) + \tau B^{-1} q(t) \tag{2.14}$$

Fig. 2.4 is an example for M-S cost function and the propagation of the curve to the interior of the object. As we can see, the curve can evolve and move of a fairly large distances, but we should say here that there is that aspect of re-gridding that you have to do; and in this context this curve was represented with around 800 control points[42].

By construction, parametric curves have a fixed topology (typically a single closed curve). Without additional splitting or merging heuristics, the curve topology will not change during the curve evolution (Fig. 2.5). In order to reach this aims, some schemes have been developed [43-45]; as disadvantages we may cite their complex algorithms and computational burden [46].

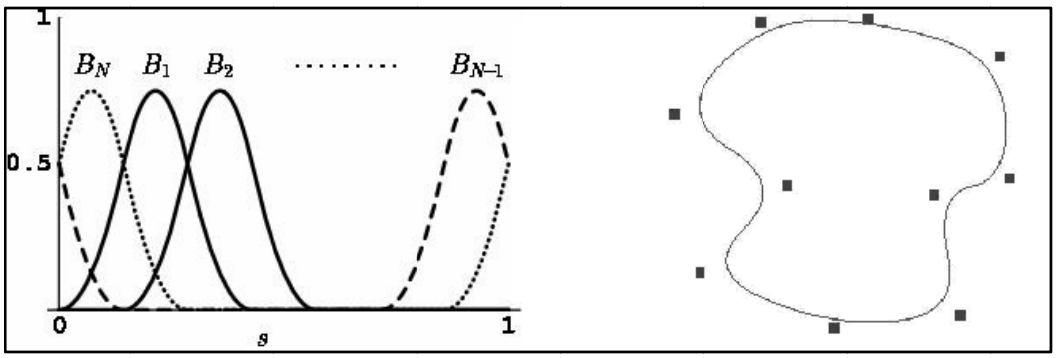

Figure 2.3: The basis functions and example of spline curve. The control points are represented by squares.

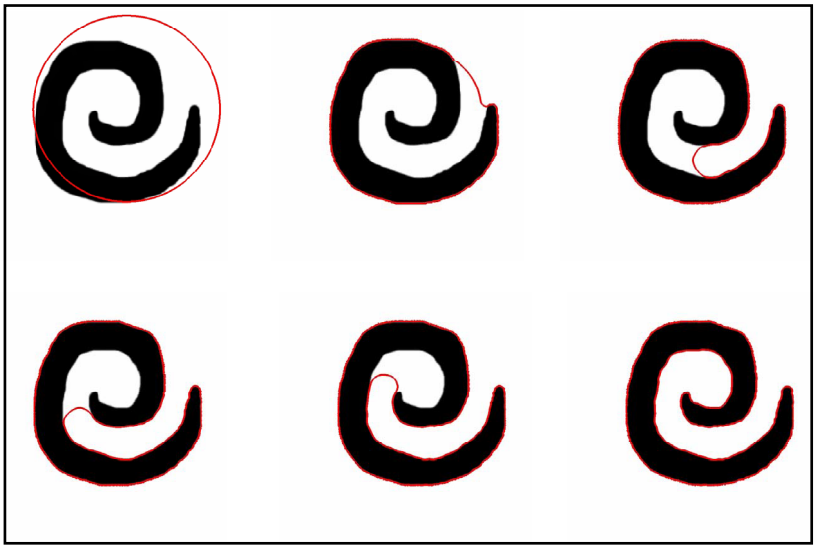

Figure 2.4: Example of propagation of the curve for M-S cost function [42].

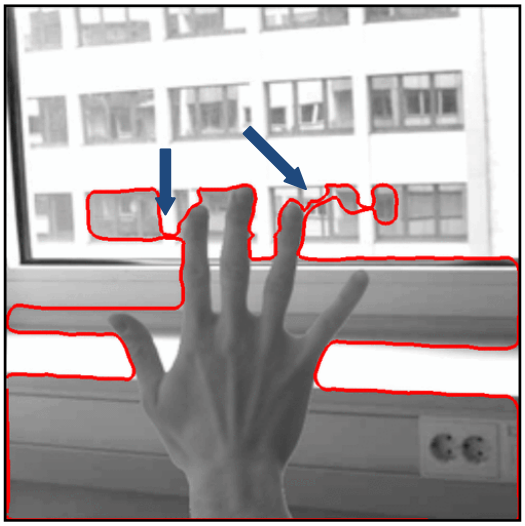

Figure 2.5: The problem of fixed topology with explicit curve evolution [42].

2.4.1.2. Implicit curve representation

Alternatively to an explicit curve representation, one can represent a curve C implicitly, for example as the zero level set of an embedding function $\Phi: \Omega \rightarrow \mathcal{R}$

$$C = \{x \in \Omega \setminus \Phi(x) = 0\} \tag{2.15}$$

Refer to Fig. 2.6, let's say the green plane is the image plane, and the red curve is the boundary that we want to represent, and we represent it implicitly by this embedding function or level set function (LSF).

This has several advantages:

+ The representation does not require a choice of parameterization.
+ The topology of the curve is not fixed.

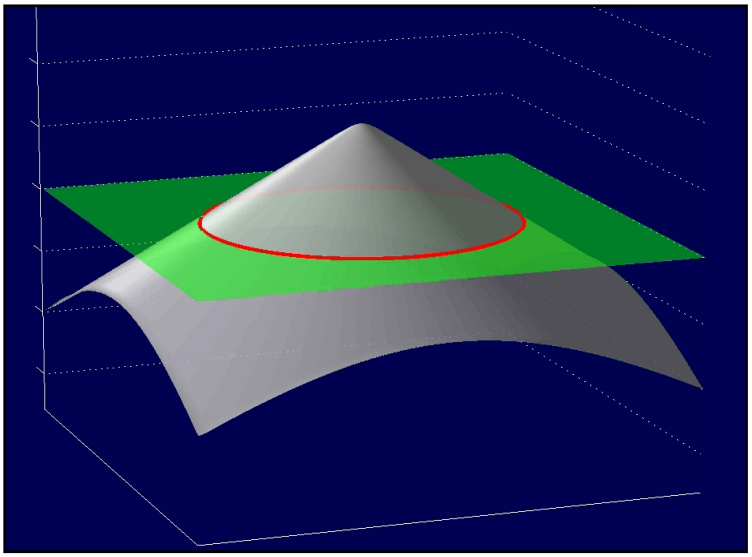

Figure 2.6: Non parametric implicit curve representation via Level set.

The evolution of curves by means of a dynamical embedding function is known as the level set method (LSM). It was first published by Dervieux and Thomasset [47] and was later reinvented by Osher and Sethian [26].

The key idea is to model the temporal evolution of a curve $C(t)$ using a family of embedding functions $\Phi(x,t)$ such that: $C(t) = \{x \, \epsilon \, \Omega \;\; \Phi(\mathrm{x},\mathrm{t}) = 0\}$.

The central question is how to evolve the embedding function Φ such that the implicitly represented curve C follows a prescribed motion.

Let the motion of the curve C be given by:

$$\frac{dC}{dt} = Fn \tag{2.16}$$

With some local speed F along the outer normal n, by definition, for any time the embedding function Φ is zero at all points of the curve.

$$\forall\, t, \quad \Phi(C(t),t) = 0 \tag{2.17}$$

As a consequence, the temporal derivative of this expression must be zero.

$$0 = \frac{d}{dt}\Phi(C(t),t) = \nabla\Phi.\frac{\mathrm{dC}}{\mathrm{dt}} + \frac{\partial\Phi}{\partial \mathrm{t}} \tag{2.18}$$

We can solve for the temporal evolution of Φ and insert (2.16) and the definition of the outer normal $n = -\frac{\nabla\Phi}{|\nabla\Phi|}$:

$$\frac{\partial\Phi}{\partial t} = -\nabla\Phi\frac{\mathrm{dC}}{\mathrm{dt}} = -\nabla\Phi\mathrm{Fn} = \nabla\Phi\mathrm{F}.\frac{\nabla\Phi}{|\nabla\Phi|} = \mathrm{F}|\nabla\Phi| \tag{2.19}$$

The above derivation shows that for a curve evolution with speed F in normal direction, the embedding function at the zero level must follow the equation:

$$\frac{\partial \Phi}{\partial t} = F|\nabla \Phi| \tag{2.20}$$

Curves can thus be evolved simply by iterating this partial differential equation called the level set equation (LSE). For visualization of the curve, one simply reads out the zero level of $\Phi(x,t)$ at any time t. Over time, this curve may undergo splitting and merging.

While the LSE specifies the motion of Φ at the boundary (curve) the evolution outside the curve location can in principle be arbitrary. Typically, one imposes that the LSF remains a signed distance function (SDF), i.e.:

$$\Phi(x,t) = \pm dist(x,C) \tag{2.21}$$

Where Φ is positive inside and negative outside the curve.

2.4.2. Level set methods for image segmentation

The first level set formulation for image segmentation were introduced in the 1990s by Casselles *et al* [19,20], Malladi *et al* [21], Kichenassamy *et al* [22]. Starting from a variational principle (snakes or M-S model) there are two alternative approaches [48]:

- **Partial Differential Equation (PDE) based ones**: where the level set evolution is directly derived from the geometric consideration of the motion equation (2.16). This was done to derive a LSM for snakes like energies known as GACs [20, 22].
- **Variational ones**: in which the variational principle is re-written with respect to the LSF (rather than the curve) and compute the gradient descent with respect to the LSF. This was proposed by Chan and Vese [24] to derive a LSM for the M-S model.

Both of these approaches are popular and both have advantages and drawbacks, the GAC is an approach for the snake, so edge-based segmentation method and C-V is proposed for the M-S, so more region-based segmentation method.

In the following, we will discuss both of these approaches.

2.4.2.1. The Geodesic Active Contours

Consider the edge-based segmentation energy:

$$E(C) = \int g(c)dc \tag{2.22}$$

It looks a little bit like the snakes in sense that we have some cost function that we integrate over the curve to undergo strong edges; the difference is that the data term $-|\nabla \mathrm{I}|^2$ in the snakes is replacing with some edge indicator function g:

$$g(x) = \frac{1}{1+|\nabla I_\sigma(x)|^2} \tag{2.23}$$

Assigning small values to strong gradients of the smoothed image I_σ. The gradient descent equation for C is given by:

$$\frac{dC}{dt} = gkn + (n\nabla g)n \tag{2.24}$$

With curvature k and normal n. the LSE is:

$$\frac{\partial \Phi}{\partial t} = |\nabla\Phi| div\left(g(x)\frac{\nabla\Phi}{|\nabla\Phi|}\right) = g.|\nabla\Phi| div\left(\frac{\nabla\Phi}{|\nabla\Phi|}\right) + \nabla g.\nabla\Phi \tag{2.25}$$

GAC is a generalization of the snakes; that its cost function is a mix of a data term and regularity; in a way that the length of the curve is cheaper in locations of strong gradient and more expansive in locations of low gradient.

Usually, the first term in the right hand side of (2.25) can be extended by replacing $div\left(\frac{\nabla\Phi}{|\nabla\Phi|}\right)$ with $div\left(\frac{\nabla\Phi}{|\nabla\Phi|}\right) + \alpha$, so that a shrinking or an expansion force, similar to the balloon force [36], is included [1].

One thing that we should mention it, that this type of level set does not compute global minima; from Fig. 2.7, the interior part of the keys should be segmented as a part of the background, and curves in this type can split and remerge but cannot jump (create curves in different locations).

2.4.2.2. The Chan and Vese LSM

In [24], Chan and Vese (C-V) proposed a LSM for the M-S energy, and in that method, interestingly curves can jump. This method is complementary to some sense to GAC in the sense that it tackles not edge-based segmentation but region-based segmentation. For the piecewise constant M-S model with two regions Ω_1 and $\Omega_2 = \Omega - \Omega_1$, and this partitioning can be represented by the LSF and more specifically, the Heaviside step function:

$$H_\Phi \equiv H(\Phi) = \begin{cases} 1, & if\ \Phi > 0\ (i.e\ x \in \Omega_1) \\ 0, & else \quad (\text{i. e x} \in \Omega_2\ ) \end{cases} \tag{2.26}$$

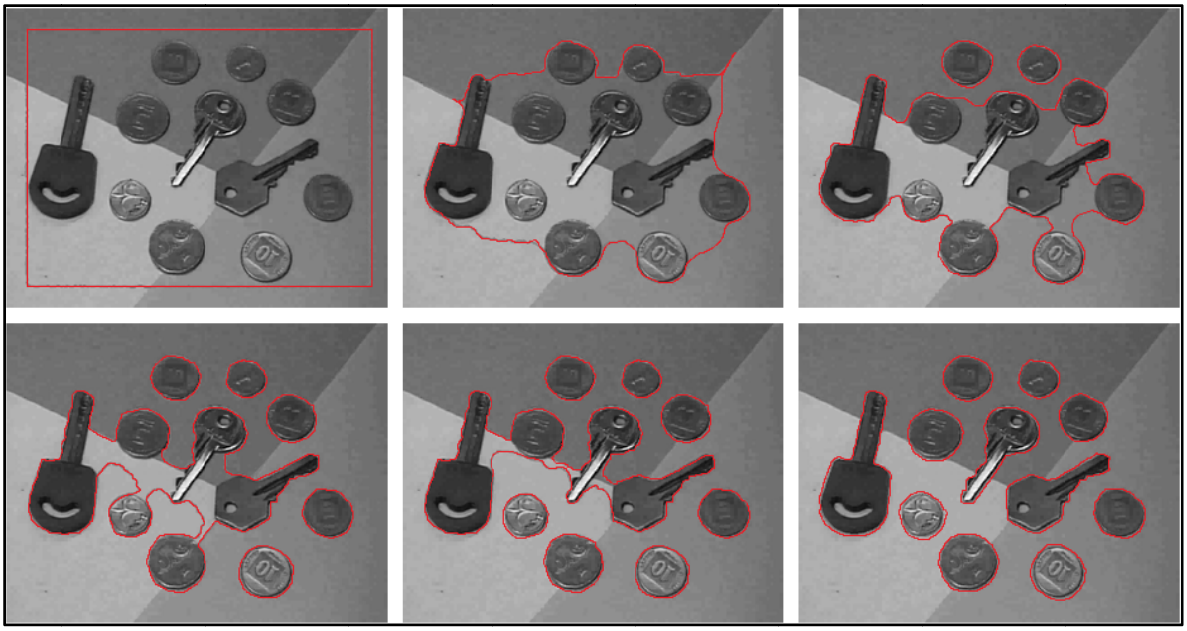

Figure 2.7: Geodesic Active Contours via Level-sets (example from [53]).

With this, we can write the M-S energy as follow:

$$E(u_i, \Omega_i) = \int_{\Omega_1} (I(x) - u_{int})^2 dx + \int_{\Omega_2} (I(x) - u_{ext})^2 dx + \nu |\delta\Omega_1| \tag{2.27}$$

$$\begin{aligned} E(u_i, \Phi) &= \int_{\Omega} (I - u_{int})^2 H_\Phi + (I - u_{ext})^2 (1 - H_\Phi) dx + \nu \int_{\Omega} |\nabla H_\Phi| dx \\ &= \int_{\Omega} (I - u_{int})^2 + (I - u_{ext})^2 \, H_\Phi + (I - u_{ext})^2 dx + \nu \int_{\Omega} |\nabla H_\Phi| dx \end{aligned} \tag{2.28}$$

Local minimization of the C-V energy can be done by gradient descent. To this end, one assumes the Heaviside step function is slightly smoothed (to make it differentiable). Its derivative is the smoothed delta function:

$$\frac{d}{d\Phi} H(\Phi) = \delta(\Phi) \tag{2.29}$$

The gradient descent equation can be computed with standard Euler-Lagrange calculus:

$$\frac{\partial \Phi}{\partial t} = -\frac{\partial E}{\partial \Phi} = \delta(\Phi)[\nu \, div \left(\frac{\nabla \Phi}{|\nabla \Phi|}\right) + (I - u_{ext})^2 - (I - u_{int})^2] \tag{2.30}$$

With $u_{int}(\phi) = \frac{\int_\Omega I(x).H(\phi)\, dx}{\int_\Omega H(\phi)\, dx}$ and $u_{ext}(\phi) = \frac{\int_\Omega I(x).(1-H(\phi))\, dx}{\int_\Omega 1-H(\phi)\, dx}$ (2.31)

For the smoothed delta function, one has various choices, for example:

$$\delta_\varepsilon(\Phi) = \frac{\varepsilon}{\pi(\varepsilon^2 + \Phi^2)} \; with \; \varepsilon > 0 \tag{2.32}$$

What's important in these examples, that this method is robust to noise and it allows jumps of the curve (Fig. 2.8). Why does the boundary jump? Strictly speaking, it doesn't; if we really have a delta function $\delta(\Phi)$, the embedding function will only move at the zero level because $\delta(\Phi)$ is zero everywhere else. But since we have a blurred version of $\delta(\Phi)$that has a certain width in the range of ε, it means that the embedding function will also move slightly inside and outside the boundary and so that, region competition term $((I - u_{ext})^2 - (I - u_{int})^2)$ will also be active everywhere in the image to create an interior boundary.

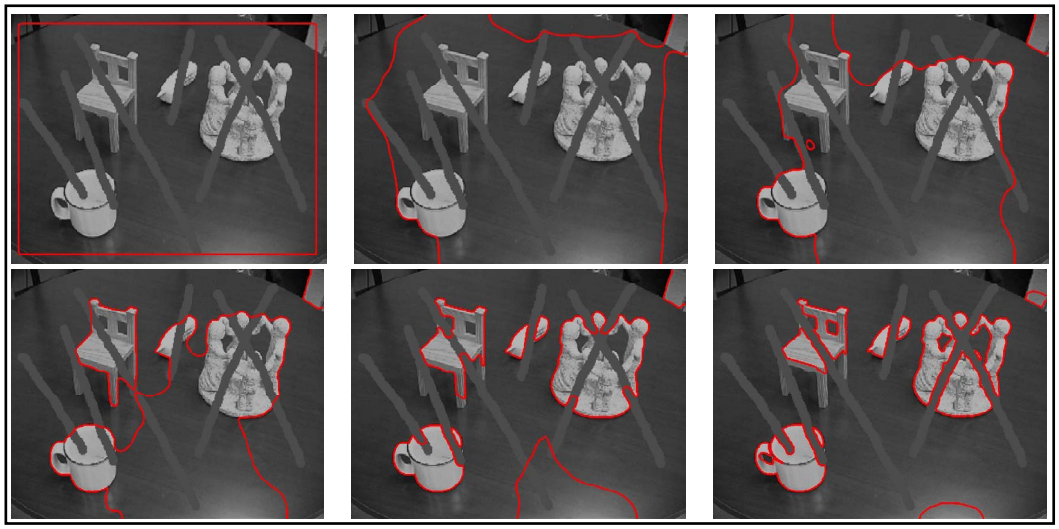

Figure 2.8: Level set evolution of the C-V model (implementation: D. Cremers).

Although this region-based model is quit robust to initializations and noise, it is build on the assumption that each region should be start statistically homogeneous that make such model sensitive to intensity inhomogeneity (Fig. 2.9).

2.5. Local region-based ACMs

In order to accurately segment and detect inhomogeneous objects, some work using local image statistics within the level set framework have been recently proposed. The key idea is to introduce a spatial window K to define the locality, suppose x and y to be two district points in image domain Ω. The local region can be defined by the following Kernel [1]:

$$K(x,y) = \begin{cases} 1 & ||x-y|| < h \\ 0 & otherwise \end{cases} \tag{2.33}$$

The local region at a given point $x \in C$ will be denoted by $\mathcal{O}(x) = \{y: ||x-y|| \} < h$. It is represented by the area inside of the blue circle shown in Fig. 2.10. Then the local neighborhood of x is divided into a local interior and exterior by the curve C. In the following, we will focus on some important local region-based ACMs.

2.5.1. Local binary fitting model

The idea of incorporating local region statistics in a variational framework begins to our knowledge with the work of Li and his co-workers [31]; the data term using the LSM is defined as follow:

$$\begin{aligned} E_{LBF}(\Phi, f_{int}, f_{ext}) = \lambda_1 \left[\int K_\sigma(x-y)\ \left(I(y) - f_{int}(x)\right)^2 H\big(\Phi(y)\big)dy\right]dx \\ + \lambda_2 \left[\int K_\sigma(x-y)\ \left(I(y) - f_{ext}(x)\right)^2 (1 - H\big(\Phi(y)\big)dy\right]dx \end{aligned} \tag{2.34}$$

Where λ_1, λ_2 are weighting positive constant. K_σ is a Gaussian Kernal Function with scaling parameter σ with a localization property that $K_\sigma(u)$ decreases and approaches zero as $|u|$ increases, and the scale parameter σ is a constant to control the local region size, f_{int} and f_{ext} are approximation of the local image intensities inside and outside the curve, respectively given by:

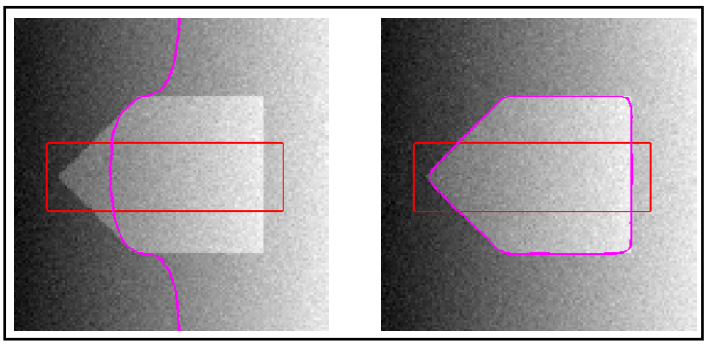

Figure 2.9: Segmentation examples of synthetic image with intensity inhomogeneity (red curve: initial contour, pink curve: result). Left: results of the C-V model, right: the LBF model [1].

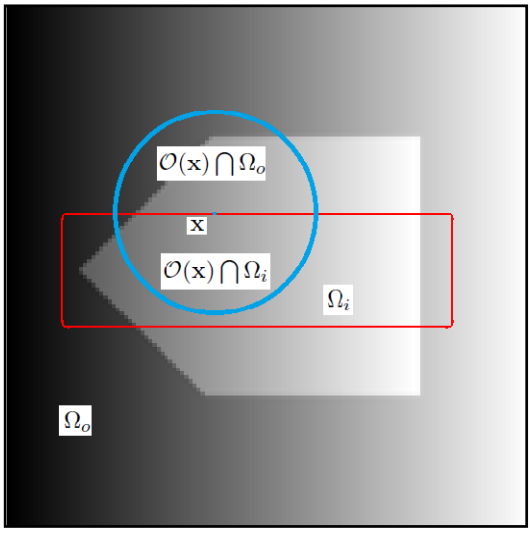

Figure 2.10: Graphical representation of local region [1].

$$\begin{cases} f_{int}(x) = \frac{\int_\Omega K_\sigma * [I(x)H(\Phi)]}{\int_\Omega K_\sigma * H(\Phi)} \\ f_{ext}(x) = \frac{\int_\Omega K_\sigma * [I(x)(1-H(\Phi))]}{\int_\Omega K_\sigma * (1-H(\Phi))} \end{cases} \quad (2.35)$$

In general, the LBF model can produce good segmentations of objects with intensity inhomogeneity. However, the LBF model only takes into account the local mean intensity information. Thus, this model is easy to be trapped into local minimum of the energy functional and the model is also sensitive to initial location of the curve [32].

2.5.2. Local Gaussian distribution fitting model

Wang *et al* [49] proposed the LGDF model by considering more complete statistical characteristics of local intensities; where these intensities are described by Gaussian distributions with different means and variances. The energy functional of this model is defined as [50]:

$$E_{LGDF}(\Phi, u_1, u_2, {\sigma_1}^2, {\sigma_2}^2) = \int -\sum_{i=1}^{2} \int w(x-y) log p_{i,x}\big(I(y)\big) M_i(\Phi(y)) dy\, dx \quad (2.36)$$

Where $M_1(\Phi) = H(\Phi)$ and $M_2(\Phi) = 1 - H(\Phi)$. $w(x-y)$ is a nonnegative weighting function, $u_i(x)$ and σ_i are local intensity means and standard deviations respectively given by:

$$u_i(x) = \frac{\int w(x-y) M_i(\Phi(y)) I(y) dy}{\int w(x-y) M_i(\Phi(y)) dy} \; and \; \sigma_i(x)^2 = \frac{\int w(x-y) M_i(\Phi(y)) (u_i(x) - I(y))^2 dy}{\int w(x-y) M_i(\Phi(y)) dy}, \; i = 1,2 \quad (2.37)$$

The LGDF model can distinguish region with similar intensity means but different variances. However it has also shortcomings as the LBF model, that is may introduce many local minimums and the result is more dependent on the initialization of the curve [51].

2.5.3. Locally statistical ACM

This model has been proposed with aim of handling intensity inhomogeneity problem and of being robust to initial contour location. It is applicable for both simultaneous segmentation and bias correction. A multiplicative model of intensity inhomogeneity is considered where the observed image $I(x)$ can be expressed as:

$$I(x) = b(x)J(x) + n(x), \quad x \in \Omega \tag{2.38}$$

Where $b(x): \Omega \to \mathbb{R}$ is the bias field which is spatially variant; $J(x): \Omega \to \mathbb{R}$ is the true signal which is assumed to be piecewise constant and $n(x)$ is the additive noise that assumed to be Gaussian distributed with zero mean and variance σ^2 [34].

In order to establish a local external energy for this model Zhang *et al* [34] first, model the distribution of intensity belonging to each object domain Ω_i as a Gaussian distribution with spatially varying means and variances:

$$p(I(y)|\alpha_i) = \frac{1}{\sqrt{2\pi}\sigma_i} \exp\left(-\frac{(I(y)-b(x)c_i)^2}{2{\sigma_i}^2}\right), y \in \Omega_i \tag{2.39}$$

Where $\alpha_i = \{b, c_i, \sigma_i\}$, σ_i is the standard derivation of intensity domain Ω_i and $b(x)c_i$ is the local mean.

Then a sliding window is used to transform the intensity domain to another domain, where the distribution overlap between different domains is significantly suppressed as observed from Fig. 2.11:

$$\bar{I}(x|\alpha_i) = \frac{1}{m_i(x)} \sum_{y \in \Omega_i \cap \mathcal{O}_x} I(y|\alpha_i) \tag{2.40}$$

Where $m_i(x) = ||\Omega_i \cap \mathcal{O}_x||$. A maximum likelihood function is defined for each point in the transformed domain, which is integrated over the entire domain to form a variational level set formulation as follow [52].

$$E(\alpha) = \sum_{i=1}^{N} \int_{\Omega} \int_{\Omega_i} \mathcal{K}_\rho(x,y)(\log(\sqrt{2\pi\sigma_i} + \frac{(I(y)-b(x)c_i)^2}{2\sigma_i^2})dydx \tag{2.41}$$

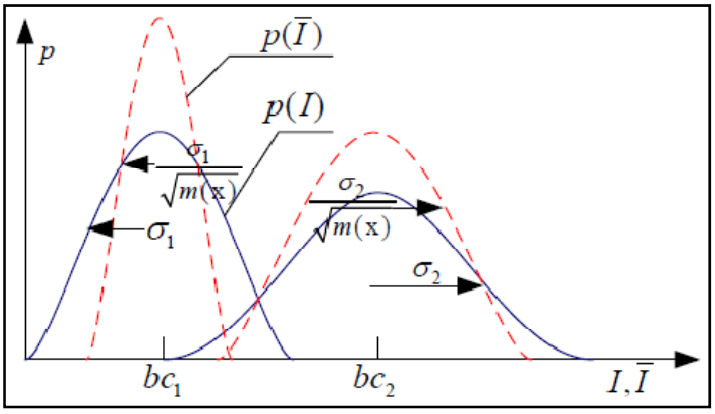

Figure 2.11: Distributions of adjacent regions in the original image intensity domain (blue solid curves) and the transformed domain (red dashed curves) [34].

Where $\mathcal{K}_\rho(x, y)$ is a kernel defined as in (2.33).

Although, this model is robust to initialization and can handle intensity inhomogeneity, it is characterized by high computational cost, in addition to the limitation of relying on a particular probabilistic model [3].

2.6. Conclusion

In this chapter, after a brief introduction to the principle of classical ACM, we have introduced geometric ACM based on the LSM, then within this framework, we introduced two different strategies using the level set method (PDE ones and variational ones) with two complementary informations (Edge-based and region-based). Edge-based approaches are applied for images with height variation in gradient at object boundaries even in the presence of intensity inhomogeneity while region-based approaches solve problems met with edge-based models such as poorly defined boundaries and noise, but they are sensitive to intensity inhomogeneity problem. We also reviewed the general framework of local region-based models and some methods that can handle intensity inhomogeneity problem. However, these models are sensitive to contour initialization to some extent, very time consuming and the results are also highly dependent on the choice of the Kernel size (size of the locality). The following chapters will introduce several possible solutions to these problems.

A Hybrid ACM without re-initialization

3.1. Introduction

Region-based ACMs are surely better alternatives to edge-based ones for images with noise or discrete edges. However, they do not often work for images with intensity inhomogeneity. Therefore, this brings out to the problem of the combination of edge and region information in one level set formulation. Facing with this problem, the rest of this chapter is organized as follow:

- We can learn several methods that regularize the LSF in its evolution, in implementing the LSM, the LSF is initialized to be a signed distance function (SDF). Since the LSF often becomes very flat or steep near the zero level, a remedy called re-initialization is applied periodically to enforce the degraded LSF being a SDF [48]. However, it is very time consuming. In recent years, some variational level set formulations [54,23] to regularize the LSF during its evolution, and hence the re-initialization procedure can be eliminated. These variational LSMs without re-initialization have many advantages over traditional methods [20,21,24], including higher efficiency and easier implementation [54].
- A first ACM which uses both edge and region information within the level set framework has been proposed by Chen *et al* [55] their approach incorporate the GAC model into the C-V model called the geodesic aided Chan Vese (GACV) model to improve the Active Contour performance on image segmentation.

Similar to this method that combine edge and region information, a hybrid model is proposed in variational level set formulation without re-initialization which consists of both gradient and region information.

3.2. LSM regularization methods

3.2.1. Re-initialization

In [26], Osher and Sethian proposed to initialize the LSF as $\Phi(x) = 1 \pm dist^2(x)$, where $dist(.)$ is a distance function and "$\pm$" denotes the signs inside and outside the contour. Later, Mulder *et al* [56] initialized the LSF as $\Phi(x) = 1 \pm dist(x)$,which is a SDF that can result in accurate numerical solutions. However, in evolution the LSF can become too steep or flat near the contour, leading to serious numerical errors. In order to reduce numerical

errors, Chopp [57] periodically re-initialized the LSF to be a SDF. Unfortunately, this re-initialization method straightforwardly computes the SDF in the whole domain and it is very time-consuming. Chopp also proposed [57] to restrict the re-initialization to a band of points close to the zero level set. Such a narrow band method [58] can reduce the computational complexity to some extent.

In summary, re-initialization has many problems, such as the expensive computational cost, blocking the emerging of new contours [48]. Therefore, some formulations have been proposed to regularize variational LSF to eliminate the re-initialization procedure [54,23].

3.2.2. Distance regularized level set evolution (DRLSE)

In [54,23], Li *et al* proposed a signed distance penalizing energy functional:

$$P(\Phi) = \frac{1}{2}\int_{\Omega} (|\nabla\Phi| - 1)^2 dx \tag{3.1}$$

Eq (3.1) measures the closeness between a LSF Φ and a SDF. By calculus of variation, the gradient flow of $P(\Phi)$ is obtained as:

$$\Phi_t = -P_{\Phi}(\Phi) = div[r(\Phi)\nabla\Phi] \tag{3.2}$$

Eq (3.2) is a diffusion equation with rate $r(\Phi) = 1 - 1/|\nabla\Phi|$. The mechanism of maintain SDF is that if $|\nabla\Phi| > 1$, we have positive diffusion rate that will decrease the gradient of the LSF, while if $|\nabla\Phi| < 1$, a negative diffusion rate is obtained and accordingly, the gradient of the LSF will be increased (Fig. 3.1).

In the rest of this chapter, we will first introduce a typical ACM which uses both edge and region information. Then our contribution will be detailed; we will concentrate on combining edge and region information on a level set framework without re-initialization. Finally, we will discuss the performance of the proposed approach with synthetic and real images.

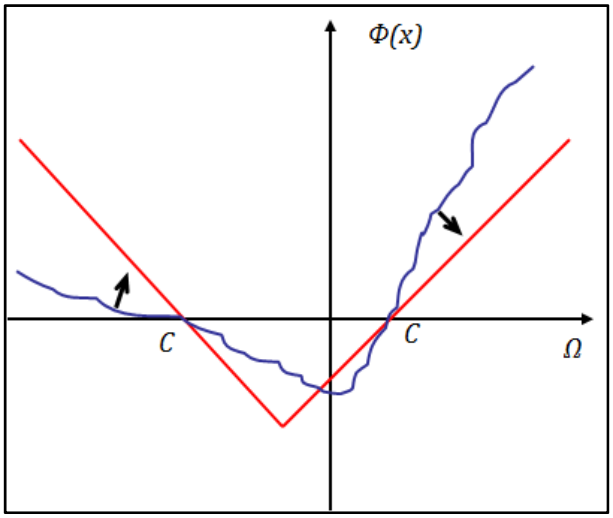

Figure 3.1: Mechanism of maintaining signed distance function [54].

3.3. Combination of edge and region information

3.3.1. Geodesic- Aided C-V method

Chen *et al* [55] have proposed to add geodesic curves advantages in the C-V model to raise ACM performance on image segmentation by inserting the ESF of the GAC model in the regularity term of the C-V model. Thus, its PDE level set formulation is:

$$\frac{\partial \Phi}{\partial t} = |\nabla \Phi| \left[\mu\, div\left(g \frac{\nabla \Phi}{|\nabla \Phi|}\right) - \lambda_i (I - C_{in})^2 + \lambda_0 (I - C_{out})^2\right]$$
$$= g|\nabla \Phi| \left[\mu\, div\left(\frac{\nabla \Phi}{|\nabla \Phi|}\right) - \lambda_i (I - C_{in})^2 + \lambda_0 (I - C_{out})^2\right] + \nabla g \,.\nabla \Phi \quad (3.3)$$

In (3.3), there are two terms in right, the first one is called the region detector and the last one is the local detector; the region detector uses statistics of homogeneous regions as in the C-V model, while multiplying $g\ |\nabla \Phi|$ as a controller of the speed evolution. The second term functions as attractive detector, which attracts the evolving curve to real boundary of objects [55]. In addition, the smoothed Dirac function $\delta_\varepsilon(\Phi)$ of the original C-V model is replaced in this approach by $|\nabla \Phi|$, which has an effective range on the whole image. In conclusion, the competition between the region detector and the attractive detector is controlled by the gradient flow (ESF) described in [20]; that is in location with high variation of gradient, the model will favor using attractive detector, while region detector is suitable for locations of small gradient variation.

3.3.2. The proposed hybrid model without re-initialization

In order to raise the performance of Active contours, edge and region information have been combined. However, the regularization of the LSF must be taken into account. To cope with this problem, we propose a hybrid edge and region ACM in a variational level set framework without re-initialization.

For a LSF Φ, we define energy functional $E(\Phi)$ by [46]:

$$E(\Phi) = \frac{1}{2}\mu \int_\Omega (|\nabla \Phi - 1|)^2 dx + \int_\Omega g|\nabla H(\Phi)| dx + \int_\Omega gF\, H(-\Phi) dx \quad (3.4)$$

The proposed Energy contain three terms, we call the first term controlled by $\mu > 0$ the penalizing term [54] that penalize the deviation of the LSF from a SDF, the second term is the edge term [23] excepted from the GAC model [20], this term is minimized when the curve is located at object boundaries, and the last term is the area term also called balloons energy [36]; this term measure the area inside the curve which speed up the motion of the curve. g is the ESF defined in [20] and F is a region detector function defined as:

$$F = (I - C_{in})^2 + (I - C_{out})^2 \quad (3.5)$$

Where C_{in} and C_{out} are the average intensities of I inside and outside the curve, respectively defined as in (2.31).

Different to the usually used balloons energy in edge-based models which is given by

$E(\Phi)_{\text{balloons}} = \alpha \int g\, H(-\Phi) dx$, depending whether α is positive or negative. The area inside the curve is favored to be large or small, and accordingly the curve will contract ($\alpha > 0$) or expand ($\alpha < 0$), while multiplying g as the controller of shrinkage or expansion of the curve. In the proposed model, inserting the region detector F in this balloon energy gives the model the advantages of the C-V model in robustness against noise and detecting discrete edges, in addition the region detector allows bidirectional motion of the curve in a single process of the curve evolution; i.e. shrinking or expanding at different location of the curve depending whether the function F is positive or negative.

In conclusion, the proposed model contains both edge and region terms by means of an implicit weight function that is the ESF; when there are any sharp edge, according to the definition of ESF in [20], it becomes very little making the region term becomes very little too, favoring use of the edge term, otherwise, the information of region acts as the main force to attract the curve to object boundaries with advantages described above.

3.4. Implementation

In practice, the Heaviside function and the Dirac function in (3.4) are approximated by smooth functions H_ρ and δ_ρ respectively, defined by the following two forms:

$$H_{1,\rho}(x) = \begin{cases} \frac{1}{2}\left(1 + \frac{x}{\rho} + \frac{1}{\pi}\sin\left(\frac{\pi x}{\rho}\right)\right), |x| \le \rho \\ 1, \quad x > \rho \\ 0, \quad x < -\rho \end{cases} \tag{3.6}$$

and

$$\delta_{1,\rho}(x) = \begin{cases} \frac{1}{2\rho}\left(1 + \cos\left(\frac{\pi x}{\rho}\right)\right), |x| \le \rho \\ 0, \quad x > \rho \end{cases} \tag{3.7}$$

Or

$$H_{2,\rho}(x) = \frac{1}{2}\left(1 + \frac{1}{2} arctan\left(\frac{x}{\rho}\right)\right) \tag{3.8}$$

and

$$\delta_{2,\rho}(x) = \frac{1}{\pi}\left(1 + \frac{\rho}{\rho^2 + x^2}\right) \tag{3.9}$$

As shown in Fig. 3.2, the support of $\delta_{1,\rho}(x)$ is restricted into a neighborhood of zero level set so that the LSF can only act locally. The evolution is easy to be trapped into local minima. In contrast, $\delta_{2,\rho}(x)$ acts on all level curves, and hence new contours can appear spontaneously, which makes it tend to yield a global minimum [24]. In the next Section, we will give some examples to show the local /global segmentation property.

The energy functional in (3.4) can be minimized by solving the following gradient flow[5]:

$$\frac{\partial \Phi}{\partial t} = \mu\left[\Delta\Phi - div\left(\frac{\nabla\Phi}{|\nabla\Phi|}\right)\right] - \delta_\rho(\Phi) div\left(g\frac{\nabla\Phi}{|\nabla\Phi|}\right) - g\,\delta_\rho(\Phi)\,F \tag{3.10}$$

[5] More details on the derivation of this equation can be found in Appendix C.

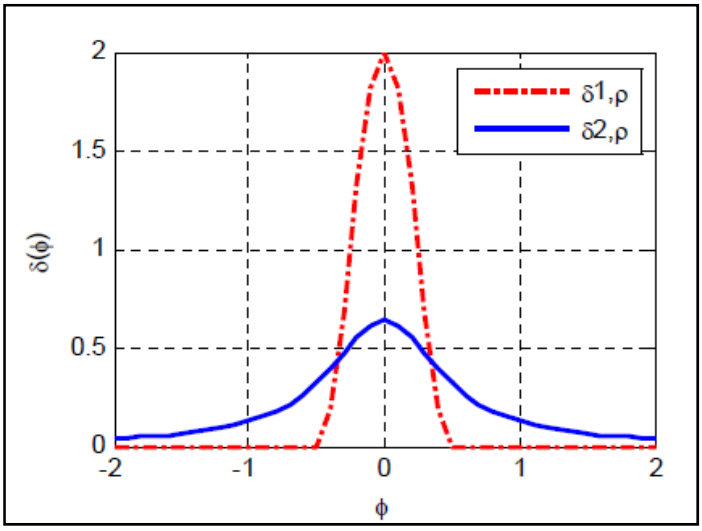

Figure 3.2: Two different regularizations delta functions [48].

The partial derivative $\frac{\partial \Phi}{\partial t}$ can be discretized using the forward differences. Thus, (3.10) is approximated as:

$$\Phi_{i,j}^{n+1} = \Delta t R(\Phi_{i,j})^n + \Phi_{i,j}^n \tag{3.11}$$

Where Δt is the time step, $\Phi_{i,j}^n = \Phi(n\Delta t, x_{i,j})$ is an approximation of $\Phi(t,x), \mathrm{x}(x_i, y_i)$ is the grid points and $R(\Phi_{i,j})$ is the approximation of the right hand side in (3.10).

The different steps, of the proposed algorithm, are as follow:

1. Initialization of the LSF Φ to be a binary function as follow:

$$\Phi_0(x,y) = \begin{cases} -d & (x;y)\ \epsilon\ \Omega_0 - \partial\Omega_0 \\ 0 & (x;y)\ \epsilon\ \partial\Omega_0 \\ +d & (x;y)\ \epsilon\ \Omega - \Omega_0 \end{cases} \tag{3.12}$$

Where $d > 0$ is a constant, Ω_0 is a subset in the image domain Ω, and $\partial\Omega_0$ be all the points in the boundaries of Ω_0.

2. Compute the ESF g, using (2.23).
3. Compute the function F, as in (3.5).
4. Compute $\Phi_{i,j}^{n+1}$ according to (3.11).
5. If $\Phi_{i,j}^{n+1}$ satisfies a stationary solution, stop, else go to step 2.

3.5. Experimental results

In this section, we compare the proposed model with the GAC model [20], the C-V model [24] and the GACV model [55]. Experiments are implemented by Matlab 7 on a computer with core i3, 3.30 GHz CPU, 4G RAM and windows 7. Unless otherwise specified, the parameters are fixed as follow: $\alpha = 0.4$ and $\sigma = 1.0$ for the GAC, $\lambda_1 = \lambda_2 = 1$ and $v = 0.8$ for C-V model, $\lambda_1 = \lambda_2 = \mu = 1$ for the GACV model, and $\mu = 0.4$, $\sigma = 1.5$ for the proposed model, $\Delta t = 0.1$ for all models.

3.5.1. Comparison with the GAC model

Fig. 3.3.A shows the convergence results with three typical initializations. The original synthetic image (gourd) with three different initial contours (inside, outside, and across the boundaries) is listed in Fig. 3.3.A(a), while the segmentation results of the GAC model (implemented with re-initialization procedure) and the proposed model are shown in Fig. 3.3.A(b) and 3.3.A(c) respectively. From Fig. 3.3.A, it is clear that the proposed model could well segment the image for the different initializations, while the GAC model fails to segment the synthetic image for the last initial contour; this is because using only edge information, and so, it cannot allow bidirectional motion (i.e., shrinking or expanding at different locations). These results illustrate the robustness of the proposed model to contour initialization.

Moreever, we add the zero-mean Gaussian white noise with a variance 0.005 to the same image of Fig. 3.3.A , and the segmentation results are shown in Fig. 3.3.B we observe that the GAC fails to detect the object and is trapped into local minima induced by gradient maxima of noise Fig. 3.3.B(b), even with increasing the size of Gaussian kernel σ, the Gaussian smoothing may remove possibly important edge and the curve will pass throught real edges of the object Fig. 3.3.B(c). Compared to the GAC model, the proposed model better capture the object, because it takes into account in its formulation the region information inserted in the area term, which is convenient with images including weak edge and noise. Furthermore, the iterations and CPU time are listed in Table 3.1. It can be observed that the proposed model is much faster than the GAC model.

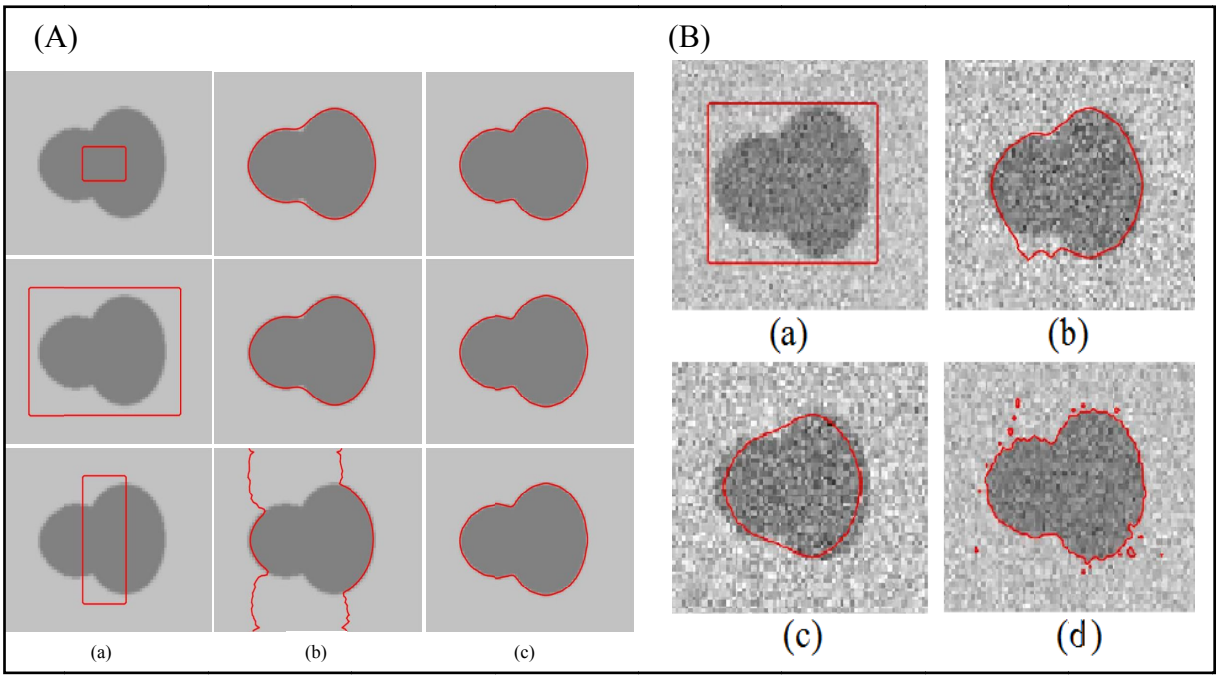

Figure 3.3: A Segmentation results for synthetic image: (a) initial contours, (b) the GAC model, (c) the proposed model. **B** Segmentation results for noisy synthetic image: (a) initial contours, (b) the GAC model, (c) the GAC model $\sigma = 3$, (d) the proposed model.

Image	Image of Fig. 3.3.A (second row)		Image of Fig. 3.3.B	
Model	GAC model	Proposed model	GAC model	Proposed model
Iterations	600	110	1500	110
Time(s)	24.67	1.84	50.01	1.84

Table 3.1: Iterations and CPU time by the GAC model and the proposed model.

3.5.2. Comparison with the C-V model

We also compare our method with the C–V model (implemented with re-initialization procedure) on a real microscope cell image where the objects boundaries are distinctive while interior intensities are not homogeneous. Fig. 3.4(a) shows the original image with initial contour and the segmentation results by the C–V model and the proposed model are shown in Fig. 3.4(b) and 3.4(c), respectively. It can be seen that the C–V model which based only on region information fails to extract the object boundary, while the proposed model achieve better results, because our model uses edge information in its energy formulation. Accordingly, it takes advantage of the GAC model.

3.5.3. Application on real images

In order to validate the proposed model, we apply it on real noisy images with different types of shapes. Four test images, shown in upper row of Fig. 3.5, which are (from left to right): a fluorescence microscopic image, MR Image of a human brain, a breast cyst image and a skin lesion image. Although, these images are corrupted by noise and / or texture tissue, the proposed model successfully can extract the desired object.

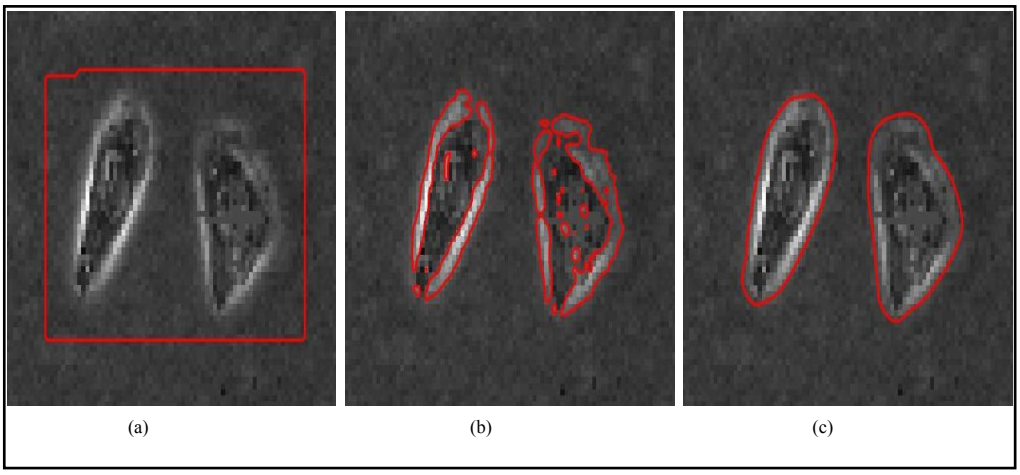

Figure 3.4: Applications to a microscope cell image: (a) initial contour. Segmentation result by: (b) the C-V model and (c) the proposed model.

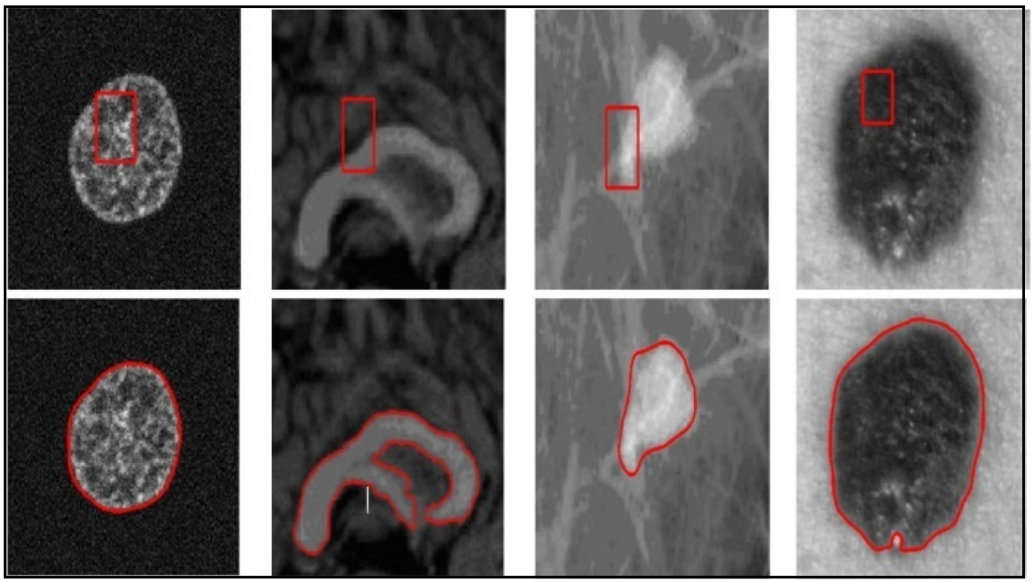

Figure 3.5: Segmentation results for real images: Row 1: original images with initial contour; Row 2: results of the proposed model.

3.5.4. Global/Local property and comparison with GACV model

Fig. 3.6 demonstrates the global segmentation property of the proposed model. The initial contour is far from all the objects (first row of Fig. 3.6). The second row shows the segmentation results using $\delta_{1,\rho}(x)$, which fails to extract all the objects, while the use of $\delta_{2,\rho}(x)$, could extract all the objects, as shown in the third row of Fig. 3.6, which is the same result with the GACV model.

Fig. 3.7 demonstrates the local segmentation property in medical image segmentation. Two magnetic resonance images of the left ventricle of a human heart are shown on the left two columns of Fig. 3.7, and the right two columns show two noisy ultrasound images of the same organ. The third row shows the corresponding segmentation results using $\delta_{1,\rho}(x)$, which are more accurate than the corresponding segmentation results when using $\delta_{2,\rho}(x)$ that are shown in the second row, which are always similar to the results of GACV model.

The proposed model is a generalization of the GACV model if we set $\delta_{\rho}(x) = \delta_{2,\rho}(x)$, which has an effective range on the whole image and the global property to detect all objects in the image.

Different to GACV model, the proposed model has the property of local segmentation when $\delta_{\rho}(x) = \delta_{2,\rho}(x)$ that is suitable when segmenting objects with intensity inhomogeneity and distinctive boundaries.

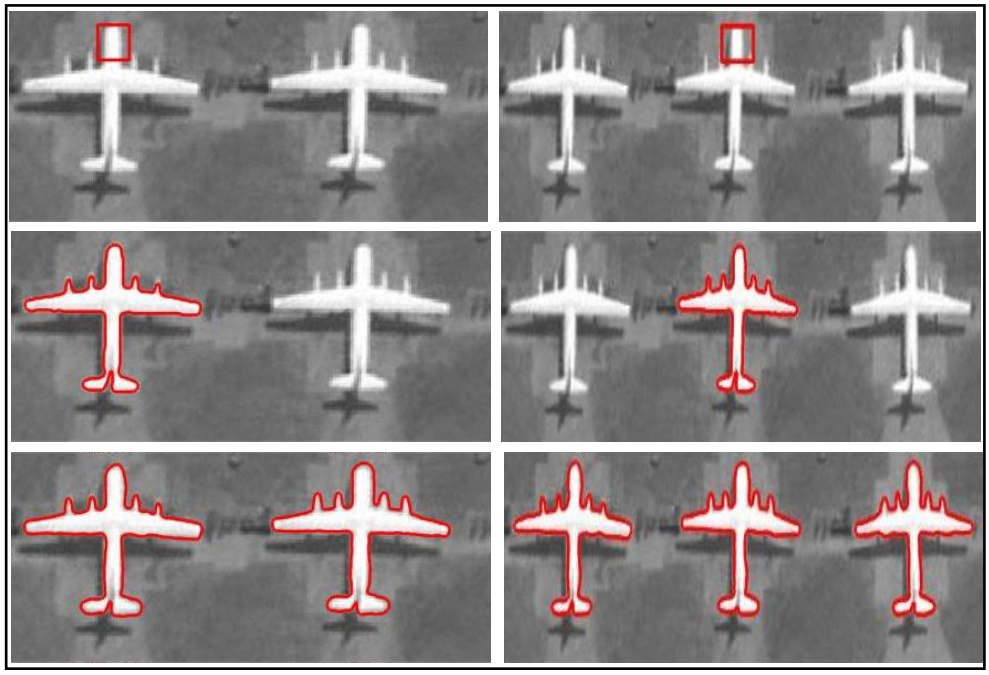

Figure 3.6: Comparisons of the global segmentation property. The first row shows the initial contours, the second row shows the segmentation results using $\delta_{1,\rho}(x)$, and the third row shows the segmentation results using $\delta_{2,\rho}(x)$.

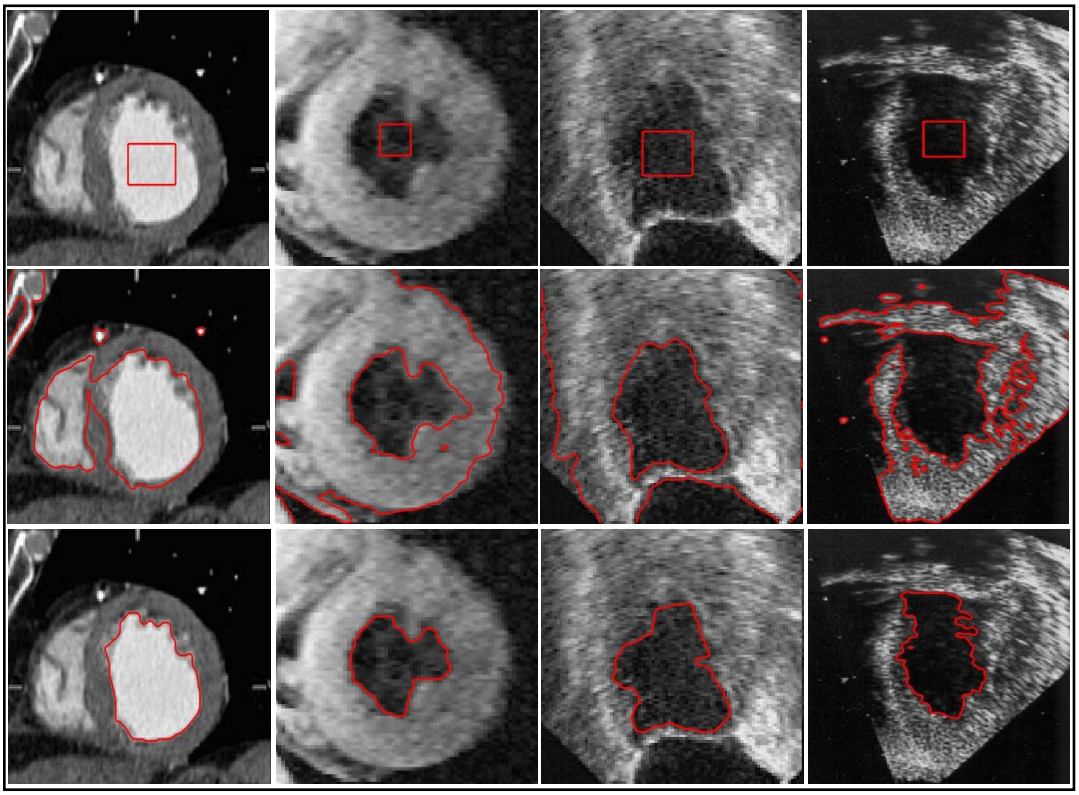

Figure 3.7: Comparisons of the local segmentation property. First row shows the initial contours. The segmentation results using $\delta_{2,\rho}(x)$are shown in the second row, and the segmentation results using $\delta_{1,\rho}(x)$ are in the third row.

3.6. Conclusion

In this Chapter, we proposed a hybrid active contour for image segmentation, in a variational level set formulation without re-initialization. The proposed model embeds both edge and region information in its energy formulation, so that, it works better than traditional edge-based and region-based methods. Experimental results on both synthetic and real images demonstrate the robustness and efficiency of the proposed model. Combining edge and region information raises the performance of active contour. However, segmenting intensity inhomogeneity problem depends on the choice of the smoothed Dirac function used, and here where local image statistics enter to the picture.

Fast region-based ACM driven by local signed pressure force

4.1. Introduction

Combining edge and region information gives the hybrid ACM the advantages of both model, but the result model still sensitive to the choice of some parameters (the smoothed delta function) and to the initialization of the curve to segment objects with intensity inhomogeneity. This leads to use another method which shares the advantages of the C-V model and the GAC; in this method a signed pressure force function (SPF) [59] is defined by statistical information substitutes the ESF in the GAC updating formulation.

A first model based on SPF was proposed by Zhang *et al* [59] to ameliorate contour initialization, this model uses region-based SPF function to update curve evolution and a special processing named Selective Binary and Gaussian Filtering Regularized Level Set (SBGFRLS) method to regularize the LSF. This model is robust and simple to implement, but it is found to be slow and parameter dependable (speed parameter) [60].

An Online region-based ACM (ORACM) using a new level set formulation was proposed in [60], which present the advantage by providing less time without changing segmentation accuracy and parameter free. Different to the ACM with SBGFRLS, ORACM uses a simple and efficient level set updating formulation by using directly current LSF instead of the curvature approximation and a simple morphological opening and closing processes instead of Gaussian smoothing to smooth the LSF. However, this model is hard to deal with the images having inhomogeneous intensity [60].

Inspired by the work in [60] and [31], we propose a fast local region-based ACM which deals well under the intensity inhomogeneity problem. It is implemented by introducing a new SPF function that utilizes the local image information provided by the LBF model in the level set updating formulation of the ORACM model. Similar to ORACM model, the proposed model uses a simple morphological opening and closing regularization operation to regularize the LSF, and in addition to ORACM model advantages, the proposed model can effectively segment images with intensity inhomogeneity. Experiments on some synthetic and real images show desirable segmentation results of our model. Moreover, comparisons with the related models also show that our model is less sensitive to initial contour location and more computationally efficient.

This Chapter is organized as follow: In section 4.2, we review some ACMs and their limitations. Section 4.3 describes the proposed model. Experimental results are shown in section 4.4. Finally, Section 4.5 concludes the Chapter.

4.2. Related methods

4.2.1. The ACM with SBGFRLS model

Zhang *et al* [59] proposed a region-based GAC which incorporates the GAC and C-V model by constructing a SPF function replacing the ESF of the GAC model. The SPF function is defined as follow:

$$SPF\big(I(x)\big) = \frac{I(x) - \frac{C_1 + C_2}{2}}{\max\left(I(x) - \frac{C_1 + C_2}{2}\right)} \tag{4.1}$$

Where C_1 and C_2 are defined as in (2.31). The SPF function modulates the signs of the pressure force inside and outside the region of interest so that the curve shrinks when outside the object, or expands when inside the object. Substituting the SPF of (4.1) for the ESF g in the GAC evolution equation (2.25), the level set formulation of this model is given as:

$$\frac{\partial \Phi}{\partial t} = SPF\big(I(x)\big)|\nabla\Phi| div\left(\frac{\nabla\Phi}{|\nabla\Phi|} + \alpha\right) + \nabla SPF\big(I(x)\big).\nabla\Phi \tag{4.2}$$

The curvature-based term $|\nabla\Phi| div\left(\frac{\nabla\Phi}{|\nabla\Phi|}\right)$ can be rewritten as $\Delta\Phi$, which is the Laplacian of the level set function Φ; the evolution of a function with its Laplacian is equivalent to a Gaussian kernel filtering the initial condition of the function. Thus this model uses a Gaussian filtering process to further regularize the level set function. Since this model utilizes a Gaussian filter to smooth the level set function to keep the interface regular, the term $|\nabla\Phi| div\left(\frac{\nabla\Phi}{|\nabla\Phi|}\right)$ is unnecessary. In addition, the term $\nabla SPF\big(I(x)\big).\nabla\Phi$ can also be removed, because this model utilizes the statistical information of regions, which has a larger capture range and capacity of anti-edge leakage. Finally, (4.2) can be written as follows [59]:

$$\frac{\partial \Phi}{\partial t} = SPF\big(I(x)\big).\alpha.|\nabla\Phi| \tag{4.3}$$

The use of the SPF function makes the model controls the direction of the evolution and to stop the evolving curve at weak or blurred edges. Moreover, the LSF of this model is regularized by the SBGFRLS which reduces the computational coast of the re-initialization step which in turn makes it more efficient than the traditional LSMs [61]. However, the ACM with SBGFRLS has two major disadvantages: the parameter α must be tuned according to images which make the model parameter dependable. The second disadvantage is slowness causes by the gradient of the level set function [60].

4.2.2. The ORACM model

ORACM [60] is a region-based active contour which covers the drawbacks provided by ACM with SBGFRLS; it necessitates no parameter and takes less time to detect objects

boundaries. Unlike the ACM with SBGFRLS, ORACM uses a simple and efficient level set updating formulation given as follow:

$$\frac{\partial \Phi}{\partial \mathrm{t}} = H\left(SPF\big(I(x)\big)\right).\Phi(x) \tag{4.4}$$

Where $H(.)$ is the Heaviside function and $SPF(.)$ is the SPF function defined in (4.1). Comparing with the level set formulation of the ACM with SBGFRLS, ORACM does not need parameters to be tuned according to input images, which make it parameter free. The directly use of current LSF instead of its curvature approximation propagates the result of the SPF on the entire current level set $\Phi(x)$ instead of its boundary $|\nabla\Phi|$. This situation leads to an increase in the current level set update rate without affecting the accuracy of the algorithm. In addition, ORACM uses a simple morphological opening and closing processes instead of Gaussian smoothing to smooth updated level set.

In spite of having a considerable amelioration from the perspective of speed and parameter dependability, using global information in the SPF function tends to erroneous segmentation results with images having inhomogeneity of intensity.

4.3. The Proposed method

Based on the level set updating formulation of the ORACM model, the proposed model is constructed by replacing the SPF function with a new SPF function, taking into account the local intensity information.

4.3.1. Local SPF function

In our model, we introduce a new SPF function based on the local properties of the image by replacing the global mean values inside and outside the curve with the local mean values provided by the LBF model. The new SPF function is called Local Signed Pressure Force (LSPF) function which is constructed as follow:

$$LSPF\big(I(x)\big) = \frac{I(x) - \frac{f_1 + f_2}{2}}{\max\left(\left|I(x) - \frac{f_1 + f_2}{2}\right|\right)} \tag{4.5}$$

Where f_1 and f_2 are defined as in (2.35).

Similar to the SPF defined in [59], the sign and value of LSPF ranges in [-1, 1] so that, it adjusts the signs of the pressure force inside and outside the region of interest so that the curve shrinks when outside the object and expands when inside the object; the only difference is that the LSPF is constructed using local mean values inside and outside the curve which help the model to work well with the intensity inhomogeneous regions, where the LSPF can be minimized when the curve is exactly on the region boundary; the local mean intensities which are computed using the Gaussian kernel as in (2.35), lead to assign different signs for both inside and outside region presenting inhomogeneous intensity.

In addition, the proposed model is a generalization of the ORACM model, and it is degenerated when the Kernel function in (2.35) is an averaging filter and the size of its window is infinity; the functions f_1 and f_2 become representing average intensities inside and outside the curve C_1 and C_2, respectively.

4.3.2. Implementation

In practice, the Heaviside function $H(.)$ in (2.35) is approximated by a smoothed functional $H_\varepsilon(.)$ defined, as proposed in [31], by:

$$H_\varepsilon(x) = \frac{1}{2}\left[1 + \frac{2}{\pi}\arctan\left(\frac{x}{\varepsilon}\right)\right] \tag{4.6}$$

Substituting the SPF function in (4.3) with the LSPF function defined in (4.4), we obtain the level set updating formulation of the proposed model as follow:

$$\frac{\partial \Phi}{\partial t} = H\left(LSPF\left(I(x)\right)\right).\Phi(x) \tag{4.7}$$

Similar to ORACM model, the proposed model uses a simple morphological opening and closing processes to smooth updated level set. These two operations performed sequentially are commonly used in computer vision and image processing for noise removal and smoothing [60].

Finally, the different steps of the proposed algorithm are as follow:

1. Initialization of the LSF Φ to be a binary function as in (3.12)
2. Compute the local mean values $f_1(x)$ and $f_2(x)$ according to (2.35).
3. Calculate the LSPF function $LSPF(I(x))$ using (4.5).
4. Evolve the level set function according to (4.7).
5. Check whether the evolution is stationary, stop, else go to step 2.
6. Regularize the LSF using a simple morphological opening and closing processes.

4.4. Results

In this section, we apply and compare the proposed model with the different models using both synthetic and real images. All models are implemented using Matlab 7.0 in Windows 7; on 3.3 GHz Intel core i3 PC with 4GB of RAM. Unless otherwise specified, the parameters are described in Table 4.1.

Fig. 4.1 shows the segmentation results of the related methods and the proposed method on a synthetic image with two objects with blurred boundaries. From the first row, we can observe that the right segmentation results cannot be obtained from the GAC model which uses edge information that causes the curve to pass over real boundaries, while the other models using region information, including the proposed one, can satisfactorily segment the two objects. Furthermore, the iterations and CPU time are listed in Table 4.2. It can be observed that both ORACM model and the proposed model are much faster than the related models. Accordingly, the proposed model is more efficient.

The second row of Fig. 4.1 demonstrates the segmentation results with tuned parameters of the related methods as follow: C-V: $\nu = 0.8$, SBGFRLS: $\alpha = 10$ and LBF: $\lambda_1 = 1.5$. As shown, they cannot detect the boundaries of the two objects after the same number of iterations mentioned in Table 4.2. While ORACM model and the proposed model, without the need of any parameter, they correctly detect the boundaries of the objects after only 5

iterations. This efficiency by the proposed method caused by using the simple level set updating formulation defined in (4.4).

Parameters	Description
d	To initialize the level set function, $d > 0$ is a constant.
σ	Scale parameter in Gaussian kernel (LBF and our model: σ determined according to images).
λ_1/λ_2	Inner/ outer weight of curve C (LBF: $\lambda_1 = \lambda_2 = 1$).
Δt	Time step (LBF, GAC: $\Delta t = 0.1$; C-V, SBGFRLS, ORACM and our model: $\Delta t = 1$).
α	Balloon force (SBGFRLS: $\alpha = 25$).
ε	The parameter of smoothed Heaviside function (LBF: $\varepsilon = 1$; our model: $\varepsilon = 1.5$).
v	Regularization parameter of curve C (C-V: $v=0.2$).

Table 4.1: Description of the parameters used in the study.

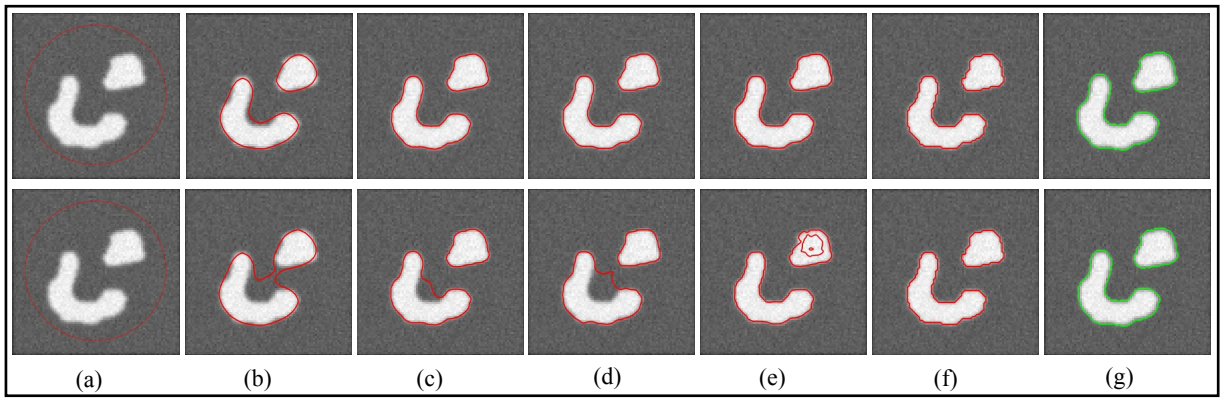

Figure 4.1: Segmentation results on a synthetic image: (a) initial contour. Segmentation result by: (b) the GAC model, (c) the C-V model (d) the ACM with SBGFRLS model (e) the LBF model (f) the ORACM model (g) the proposed model. The parameter $\sigma = 30$.

Method	Iterations	CPU time (s)
The GAC model	2000	72.44
The C-V model	80	5.22
The ACM with SBGFRLS model	25	3.30
The LBF model	10	2.33
The ORACM model	5	1.71
The Proposed model	5	1.71

Table 4.2: Iterations and CPU time needed by the methods compared when segmenting the image in Fig. 4.1.

To demonstrate the local segmentation property of the proposed model, in Fig. 4.2 we compare our method with the related methods on a real microscope cell image where the objects boundaries are distinctive while interior intensities are not homogeneous. It can be observed that the GAC model based on edge information can extract the objects boundaries, while other related methods which are based on region information fail to extract them. Compared to the related models based on region information, the proposed model achieve better results, because our model uses local signed pressure force in its level set formulation that has the property of local segmentation.

Fig. 4.3 shows a segmentation result comparison with the related methods on image with intensity inhomogeneity. It can be seen that the methods using global region information (C-V, SBGFRLS and ORACM) cannot segment well when image has intensity inhomogeneous region in it, while the LBF model and the proposed method that uses local region information, could accurately segment intensity inhomogeneous region. For the GAC which based on edge information where no global constraints are placed on the image, this method can segment intensity inhomogeneity but suffer from the leakage problem as shown in Fig. 4.3(b).

In the next experiments, we will focus on comparisons between the LBF model and the proposed model on intensity inhomogeneity problem from different sides.

In Fig. 4.4, we apply the LBF model and the proposed model to a synthetic image with intensity inhomogeneity, the first row shows various initial contours, the second and the third rows show the segmentation results by the LBF model and the proposed model, respectively. From some initial contours, as in columns 1 and 5, the LBF model can segment well intensity inhomogeneity image, while giving bad segmentation results for other initial contours. Otherwise, the proposed model is much more robust to initial contour location and can achieve good segmentation results for all initial contours.

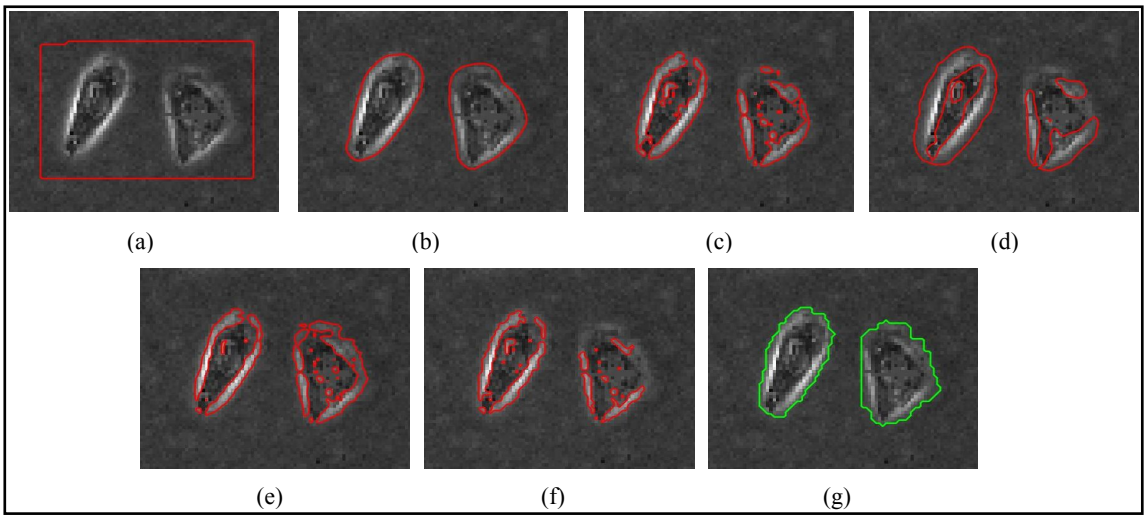

Figure 4.2: Applications to a microscope cell image (downloaded from [23]): (a) initial contour. Segmentation result by: (b) the GAC model, (c) the C-V model (d) the ACM with SBGFRLS (e) the LBF model (f) the ORACM model (g) the proposed model. The parameter $\sigma = 4$.

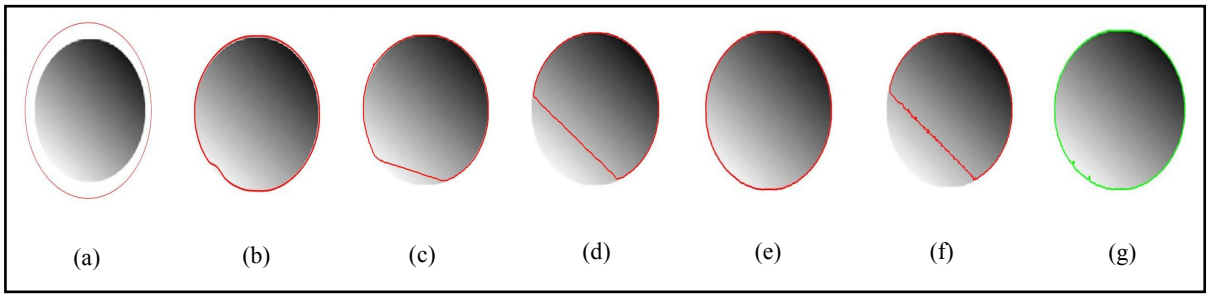

Figure 4.3: Comparison of segmentation results using synthetic image with intensity inhomogeneity (downloaded from [62]): (a) initial contour. Segmentation result by: (b) the GAC model, (c) the C-V model (d) the ACM with SBGFRLS (e) the LBF model (f) the ORACM model (g) the proposed model. The parameter $\sigma = 2$.

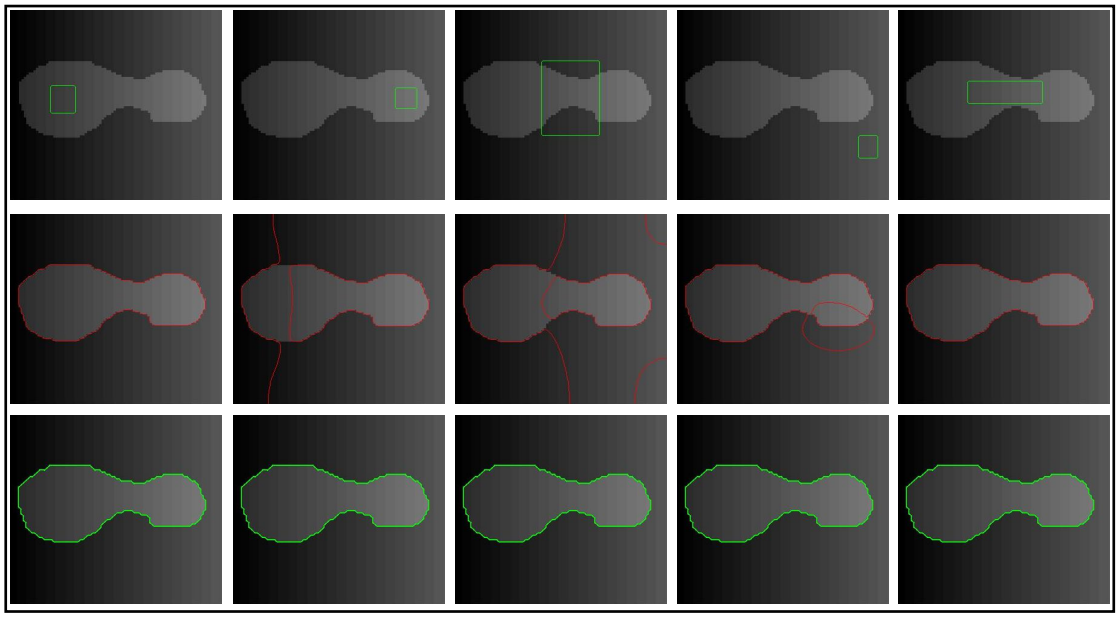

Figure 4.4: Segmentation results on the synthetic image with intensity inhomogeneity. Row1: initial contours. Row2: results of the LBF model. Row3: results of the proposed model. The parameter $\sigma = 5$.

In order to compare the LBF model and the proposed model, we use other synthetic images in Fig. 4.5 and Fig. 4.6.

Fig. 4.5(a) shows the original image with initial contour. The results of the LBF model and the proposed model are shown in Fig. 4.5(b) and 4.5(d), respectively. It is obvious that the proposed model attains better segmentation precision; it separates the boundary of each finger of the palm and reflects its shape (as can be seen clearly in the zoomed view of Fig. 4.5(e) better than the LBF model (zoomed up in Fig. 4.5(c)).

Fig. 4.6 shows the segmentation results of another synthetic image with intensity inhomogeneity by the LBF model and the proposed model, which are shown in Fig. 4.6(b) and 4.6(c) respectively, while Fig 4.6(a) shows the original image with initial contour. From the results, it is clear that the LBF model fails to get the correct segmentation result and traps into local minimum, while the proposed model gets right segmentation result.

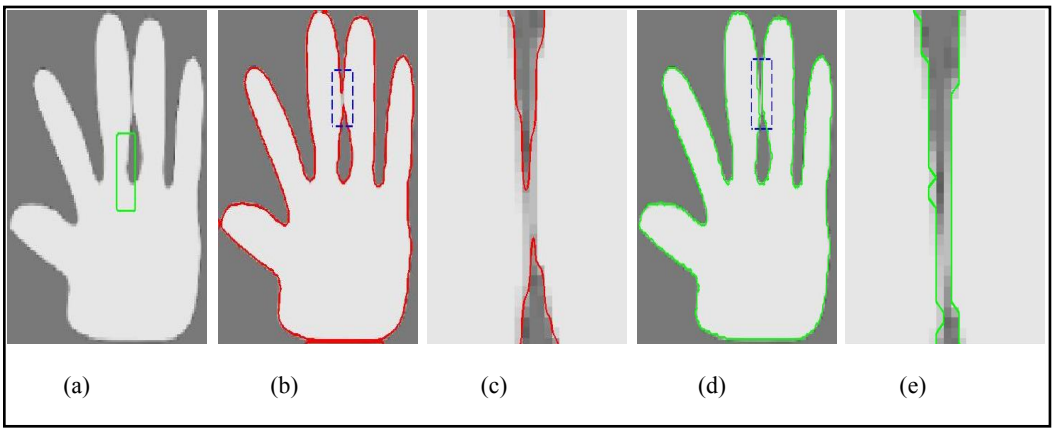

Figure 4.5: Segmentation results on a hand phantom (downloaded from [59]) using the LBF and the proposed model: (a) initial contour, (b) segmentation result by the LBF model, (c) zoomed view of the narrow, blue rectangle in (b), (d) segmentation result by our method, and (e) zoomed view of the narrow, blue rectangle in (d). The parameter $\sigma = 3$.

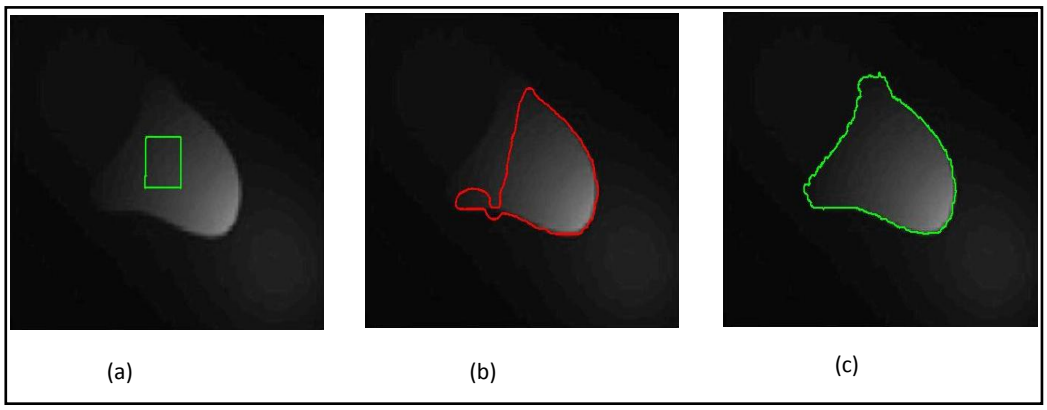

Figure 4.6: Segmentation results of an inhomogeneous image (downloaded from [63]). (a) The original image with initial contour, (b) the final contour with the LBF model and (c) the final contour with the proposed model. The parameter $\sigma = 30$.

To furthermore compare the performance of the proposed model and the LBF model, on images whose intensity inhomogeneity has different strength. Fig. 4.7 shows the segmentation results provided by the LBF model (first row) and the proposed model (second row), on five synthetic images with different intensity inhomogeneity. Clearly, the proposed model can segment the object with different strength of intensity inhomogeneity, while the LBF model fails to segment the object when the strength of intensity inhomogeneity is strong (last two Columns).

To quantitatively validate the segmentation performance of the proposed model from Fig 4.7, the Jaccard Similarity (JS) index is used. The JS index between the segmented object region Rs and the real object region Ro is calculated as $JS(R_S, R_O) = |R_S \cap R_O| \,/\, |R_S \cup R_O|$. Clearly, when R_S is more similar to R_O, the JS value is close to 1. Fig 4.8 shows that the JS values obtained by our method change in a small range for intensity inhomogeneity with different strength, while the LBF model, when the strength of intensity inhomogeneity is strong (last two columns of Fig 4.7) the segmentation accuracy of this method decreases strictly. These results illustrate the robustness of the proposed model to image intensity inhomogeneity.

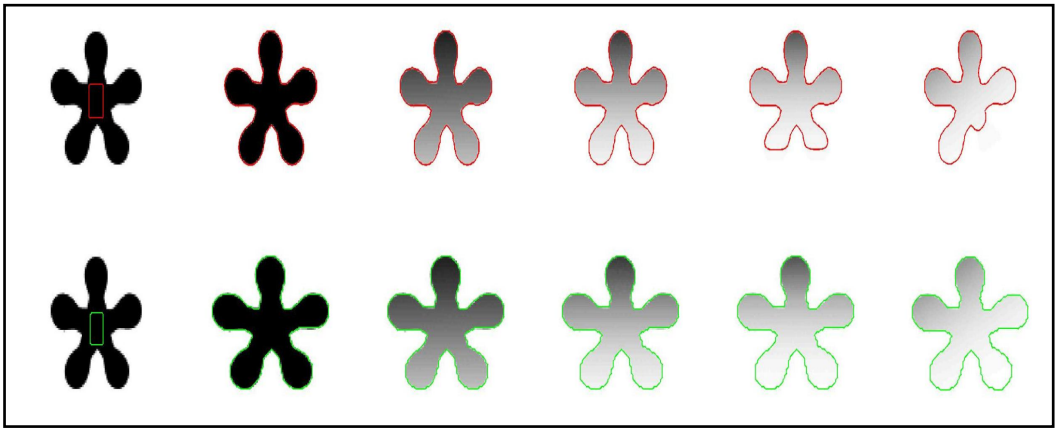

Figure 4.7: Segmentation results on a synthetic image where the strength of intensity inhomogeneity is gradually increased from left to right (downloaded from [64]). Row1: results of the LBF model. Row2: results of the proposed model. The parameter $\sigma = 2$.

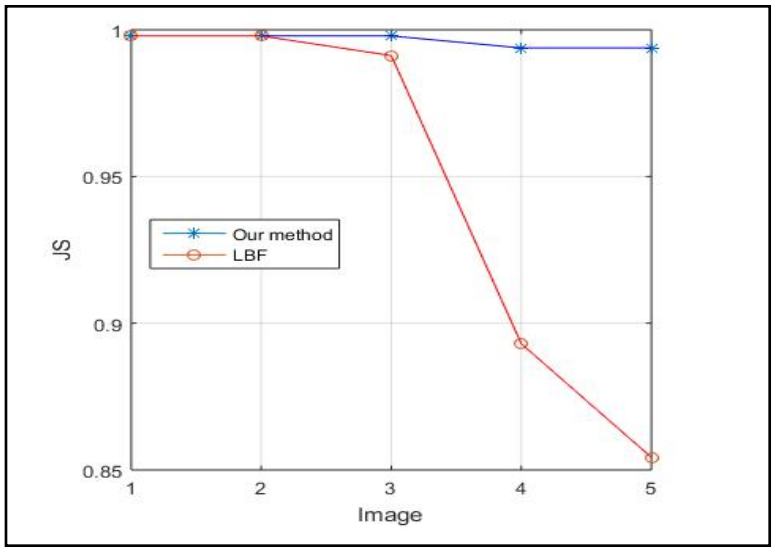

Figure 4.8: The corresponding JS values yielded by the LBF model and the proposed model on the five images with different intensity inhomogeneity.

In Fig 4.9, we apply the proposed model to segment typical medical images with different modalities and compare it to LBF model. The segmentation results provided by the LBF model are in the upper row, while the lower row presents our results. The first two columns show the results of two X-ray images of blood vessels. It can be seen that all models give satisfying segmentation results because of the use of the image local region information, which can better separate the object from background. The last three columns, from left to right, show the segmentation results of a CT image of heart and two MRI brain images with intensity inhomogeneity. It can be seen that the LBF model fails to distinguish between the intensity between the object and its background and lead to inaccurate segmentation result. While the proposed model gives much better segmentation results. These results represent the abilities of the proposed model to deal with intensity inhomogeneity and complex background.

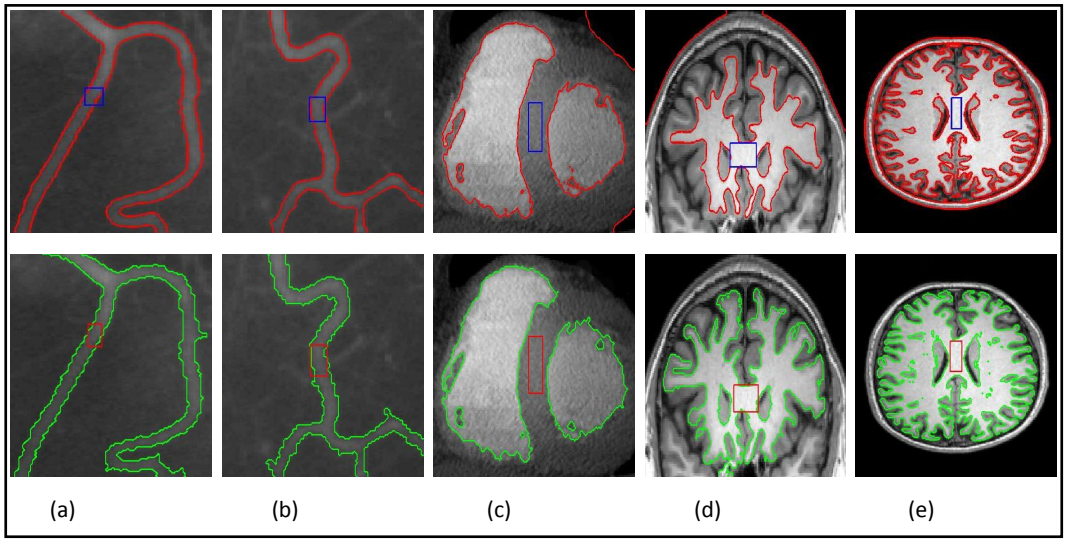

Figure 4.9: Comparison of segmentation results of the LBF model (top row) and the proposed model (bottom row) on several medical images (a, b, d and e: downloaded from [64], while c: from [33]).

Furthermore, the iterations and CPU time of segmenting the images in Fig 4.9, moreover the values of the parameter σ are listed in Table 4.3 for the LBF model and the proposed model. It can be observed that the number of iterations and the required CPU time of the proposed model are much less than those of the LBF model. Accordingly, the proposed model is much faster than the LBF model.

To compare the performance between the LBF model and the proposed model on noisy image, we add the salt and pepper noise with various levels on the synthetic image of Fig. 4.4, and the segmentation results are shown in Fig. 4.10; the first column shows the original image with initial contour, the second, third and fourth Columns show the segmentation results on image added noise with densities: 0.05, 0.1 and 0.2 respectively. From the results, it is obvious that the proposed model has higher anti-noise than the LBF model; this performance is because of using the opening and closing morphological operations respectively to remove small objects and to smooth the active contour.

Finally, Fig. 4.11 shows the influence of the parameter σ on the segmentation results of our model for an MR image of bladder with intensity inhomogeneity. The initial contour is shown in Fig 4.11(a) and the results for the parameter $\sigma = 8$ and $\sigma = 30$ are shown in Fig 4.11(b) and 4.11(c), respectively. It is clear that the corresponding result with $\sigma = 8$ is more desirable, where the bladder and all small structures surrounding it are segmented. While some part of the bladder and these structures are missed in the segmentation result using $\sigma = 30$, which is similar to the result of the ORACM model, shown in Fig 4.10(d). As an advantage of the proposed method from these results, that it allows the choice of the scale parameter σ to exploit intensity information in regions of different scales, so that, when the intensity inhomogeneity is severe, the accuracy of segmentation relies on the local SPF, in such case, we choose small σ, while in smooth regions, a bigger σ is chosen; the local SPF becomes degenerating the global SPF so that the contour is attracted to the object boundary quickly.

Method	The LBF model			The proposed model		
Figure	Parameter σ	iterations	CPU time (s)	Parameter σ	iterations	CPU time (s)
Fig. 9(a)	4	160	3.43	7	3	0.55
Fig. 9(b)	4	120	2.04	10	11	1.55
Fig. 9(c)	10	300	10.06	10	10	1.40
Fig. 9(d)	3	60	5.06	10	4	1.01
Fig. 9(e)	5	100	10.08	25	4	1.39

Table 4.3: Iterations, CPU time and values of σ needed when segmenting the images in Fig 4.9.

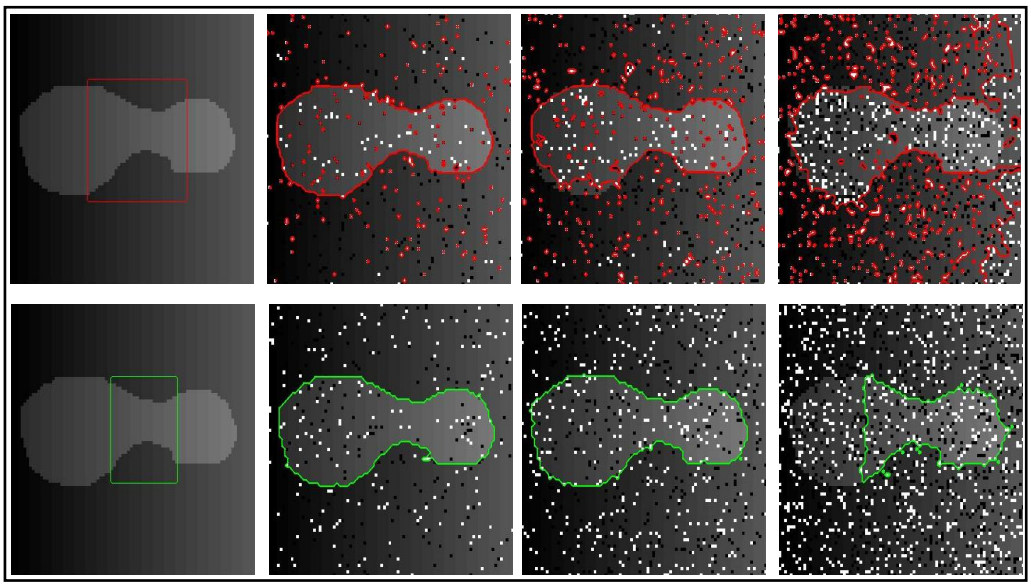

Figure 4.10: Comparisons of the segmentation results with salt and pepper noise by the LBF model and the proposed model on Row1 and Row2, respectively. Column1: the original image with initial contour; Columns 2, 3 and 4 added the salt and pepper noise with densities 0.05, 0.1 and 0.2, respectively. The parameter $\sigma = 10$.

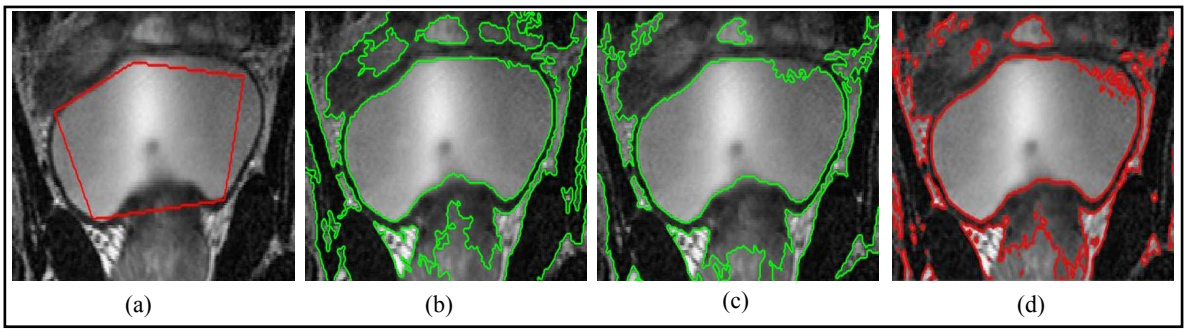

Figure 4.11: Experiments on an MR image of bladder (downloaded from [31]): (a) Initial contour. Result of our model for: (b) $\sigma = 8$. (c) $\sigma = 30$. (d) Result of the ORACM model.

4.5. Conclusion

In this Chapter, a region-based active contour method for image segmentation is presented which can efficiently segment the images with intensity inhomogeneity by exploiting the local image information. In particular, A new SPF function is constructed which uses local mean image information provided by the LBF model and helps to segment intensity inhomogeneous regions. Experimental results on both synthetic and real images demonstrated the advantages through accuracy, rapidity and insensitivity to the initial contour location of the proposed model over the related models.

Although using local SPF overcomes the sensitivity of local region-based method to curve initialization and to noise when segmenting image with intensity inhomogeneity, its result is sensitive to the choice of size of the locality. Edge-based models of highly localized image information, based on gradient information are adequate in segmenting intensity inhomogeneity, but they are found to be sensitive to image noise and poorly defined boundaries. The following chapter will introduce possible solution to these problems, such as the use of texture analysis in constructing new edge stopping function.

Robust ACM guided by local binary pattern stopping function

5.1. Introduction

To solve problems met with ESF based on gradient information, we propose a stopping function based on the Local Binary Pattern (LBP) textons [65,66]. This new function is called LBP stopping function (LBPSF). The LBP textons was originally used to perform adaptive gradient calculation for edge detection [67] in which, the LBP textons is used to classify regions of an image around a pixel into noisy, homogenous and edge regions, and then, accordingly, an adaptive filter is introduced while calculating the gradient.

The classification of the image regions into: noisy, homogeneous and edge regions using the LBP textons, helps to generate a filter rejecting pixel positions of LBPs which are likely to be produced by noise and calculate gradient magnitudes at the accepted pixel positions to detect the edges using a modified canny edge detector based on LBP, and then, constructing a LBPSF which takes values of "1" on noisy and homogeneous regions, while having values of "0" on edges. Consequently, the curve will stop at these edges. Substituting the ESF based gradient information of the GAC model [20] with the proposed LBPSF in a variational formulation; we obtain a fast ACM which is robust to the leakage and noise problems.

The rest of this Chapter is organized as follow: Section two presents a theoretical background of the LBP and introduces the derivation of the LBPSF and the proposed ACM based on it. Section three provides experimental results and comparisons to the models proposed in [20], [60] and [34]. Finally, Section four concludes the Chapter.

5.2. The proposed method

5.2.1. Local binary pattern

The LBP operator was first introduced by Ojala *et al* [65] and Mäenpää [66] for texture analysis. It has been applied in many active studies such as texture classification and face recognition [68]. The LBP operator combines characteristics of statistics and structural texture analysis; it describes the texture with primitives called textons [69].

The derivation of an LBP code is shown in Fig. 5.1(a); taking a neighbourhood of 3×3 of a central pixel, thresholding it into two levels "0" or "1" whether the neighbour of that

pixel has smaller or larger value than the central pixel, respectively. An LBP code is obtained by multiplying the threshold values of eight pixels with binomial weights and summing up the result. This leads to the equation:

$$LBP_{P,R} = \sum_{P=0}^{P-1} s(g_P - g_c)2^P \tag{5.1}$$

Where P is the number of neighbours, R is the radius, g_c corresponds to the gray value of the center pixel, g_P are the gray values of surrounding pixels and $s(x)$ is given by:

$$s(x) = \begin{cases} 1, & x \geq 0 \\ 0, & x < 0 \end{cases} \tag{5.2}$$

Different texture primitives can be detected by the LBP code, Fig. 5.1(b) shows examples where ones and zeros are indicated with white and black circles respectively. A special kind of LBP, which will be used for edge detection, is called rotation-invariant uniform LBP giving by:

$$LBP_{P,R}^{riu2} = \begin{cases} \sum_{P=0}^{P-1} s(g_P - g_c)2^P, if\ U(LBP_{P,R}) \leq 2 \\ P+1, else \end{cases} \tag{5.3}$$

Where U is the number of bitwise 0/1 and 1/0 transitions in an LBP, only two or less are allowed for uniform LBP [67]. Fig. 5.2 shows the nine classes of the uniform LBP.

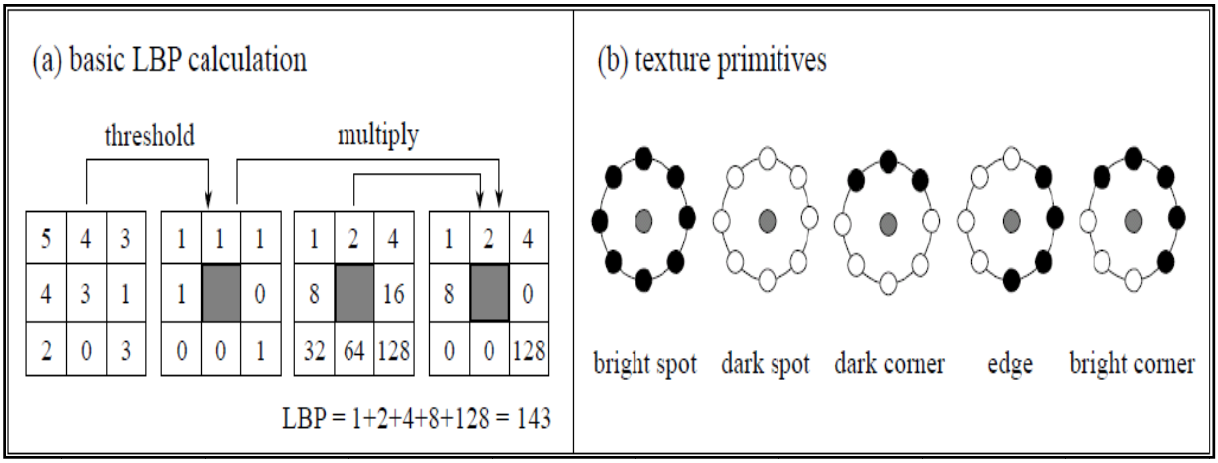

Figure 5.1: Calculation and interpretation of Local Binary Patterns (LBPs) [67].

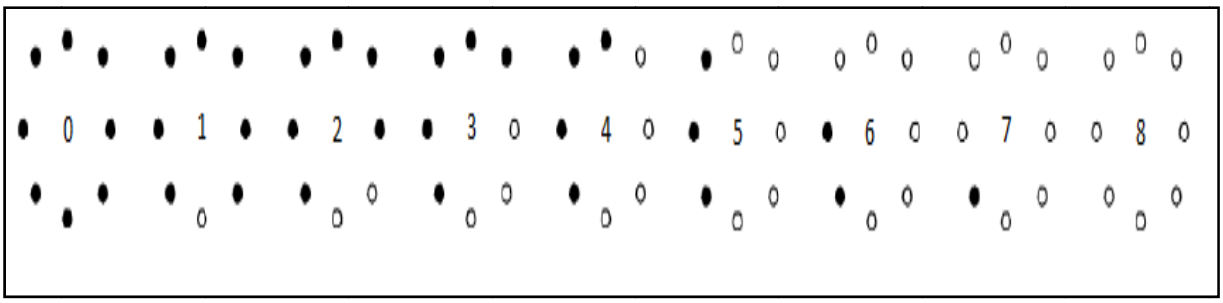

Figure 5.2: Classes of the non uniform rotation invariant LBPs.

5.2.2. Edge detection with LBP

For some example images with different levels and types of artificial noise, Teutsch *et al* [67] have calculated $LBP_{P,R}^{riu2}$ with variable radius R for each pixel and accumulated in LBP histograms. Each histogram has ten bins: nine for the different $LBP_{P,R}^{riu2}$ equivalence classes, which are displayed in Fig. 5.2, and one for all other LBPs. From Fig 5.3, it can be seen that the number of edges of different orientations ($LBP_{P,R}^{riu2}$classes 2-6) decreases when the noise level increases while other LBPs (classes 0, 1, 7, 8 and 9) are much affected by noise [70].

The main idea in this approach is that all pixels of those classes affected by noise are not considered for gradient calculation in edge detection and then, accordingly, noise can be suppressed. Edge detection using LBPs is based on the Canny edge detector algorithm with modified steps as follow:

5.2.2.1. Noise suppression

Unlike in Canny's algorithm where noise is suppressed by smoothing with Gaussian kernel, in this approach, a filter is generated which rejects pixel positions of LBPs which are likely to be produced by noise (classes 0, 1, 7, 8 and 9); a binary function f is applied pixelwise to all image pixel positions *c=(x, y)* of the following formula:

$$f(c) = \begin{cases} 1 \; if \; LBP_{P,R}^{riu2} \; \epsilon \; classes \; (2-6) \\ 0, else. \end{cases} \tag{5.4}$$

Only pixel positions with $f(c) = 1$ will be considered for the next step.

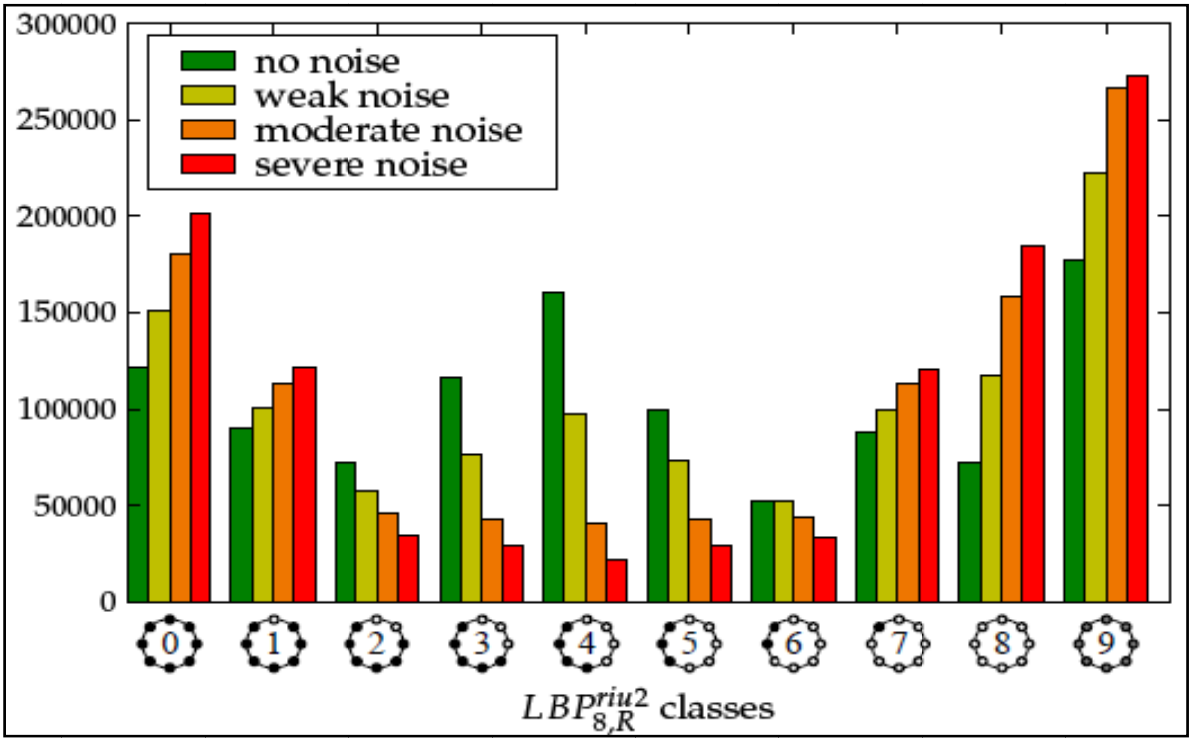

Figure 5.3: LBP histogram for Lena with different noise levels [70].

5.2.2.2. Gradient magnitude

Gradient magnitudes $G(c)$ in this approach are calculated at the accepted pixel positions $(f(c) = 1)$ using the local variance $VAR_{P,r}$:

$$G(c) = \begin{cases} \sum_{r=R_1}^{R_n} \sqrt{VAR_{P,r}}, if\ f(c) = 1 \\ 0, else, \end{cases} \tag{5.5}$$

Where r is the variation of the radius R to calculate several LBPs and summed up for the gradient magnitude in order to increase the robustness against noise. Variance tends to focus too much on bright objects. So, standard-deviation is used instead of variance as it produces more homogeneous edge images [67]:

$$VAR_{P,r} = \frac{1}{P}\sum_{p=0}^{P-1}(g_P - \mu)^2 \quad \text{where} \quad \mu = \frac{1}{P}\sum_{p=0}^{P-1} g_P \tag{5.6}$$

5.2.2.3. Non-maximum suppression

As in Canny's algorithm, four discretized gradient orientations: 0°, 45°, 90°, and 135° are used. While these orientations are calculated using the *atan2* function in Canny, this approach doesn't need to calculate anything in order to get the orientation. Instead, four sets: D^0_{LBP}, D^{45}_{LBP}, D^{90}_{LBP} and D^{135}_{LBP} of LBP that represent the orientations are simply defined. Each set D consists of 16 LBP as in Fig. 5.4. Since LBP with an even number of bright/dark dots are ambiguous, we simply say that they belong to two sets [67].

5.2.2.4. Determination of edge pixels

The final step is to generate a binary edge pixel image *B* using the hysteresis operator, in which pixels are marked as either edges, non edges and in-between, this is done based on two thresholds t_1 and t_2 with $t_1 < t_2$. If a gradient magnitude *G(c)* exceeds t_2, it is accepted as edge pixel, while all pixels with gradient value less than t_1 are marked as non edges. The next step is to consider each of the pixels that are in-between, if they are connected to edge pixels these are marked as edge pixels as well. The result of this edge detector is the binary image *B* in which the white pixels closely approximate the true edges of the original image.

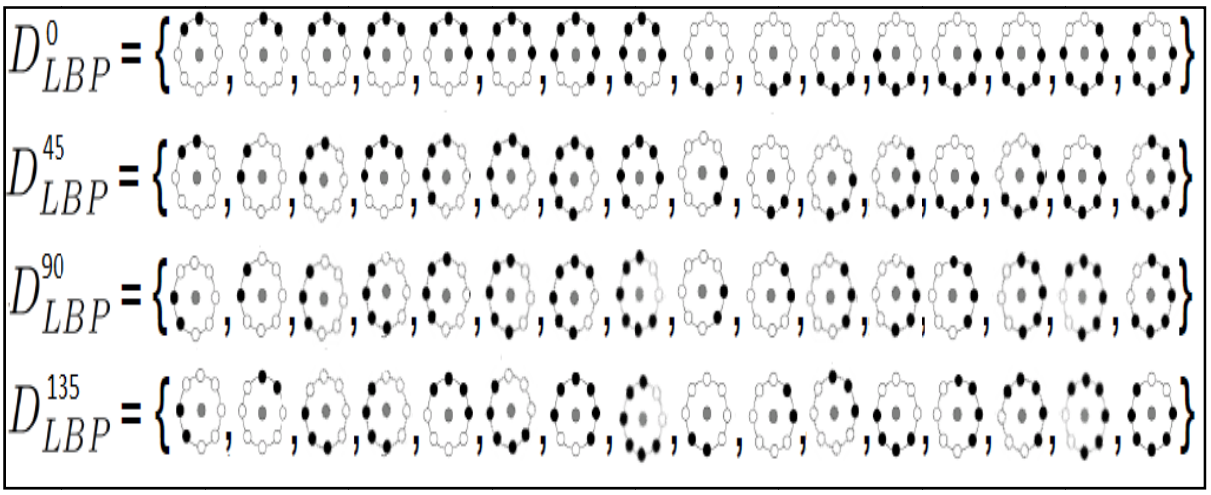

Figure 5.4: The four sets with LBPs of different orientations.

5.2.3. The ACM based LBP stopping function

We firstly introduce the LBPSF and to motivate it, we will present the classical ESF and some of its shortcoming.

The philosophy behind the edge-based ACM is finding curve that undergoes strong edges (object boundaries), and to achieve this goal, an external energy is defined that we integrate over the curve to move it toward the object boundaries.

Let *I* be a given gray level image, the classical ESF is defined as in (2.23). This function assigns small values to strong gradients of the smoothed image $\nabla G_\sigma * I$ where the curve is very close to the boundaries. However, these gradient based functions have two major drawbacks:

In practice, the discrete gradients are bounded and then, the function g can be relatively far from zero on the edges and the curve may pass through the boundaries [24,27].

The next issue is that for the noisy or textured regions, the image will have gradient maxima which induce local minima in the external energy. Therefore, the curve will not stop at the real object's boundaries. Alternatively, the Gaussian smoothing is used to remove spurious local minima. Yet, smoothing also removes possibly important edge information if the kernel width σ is not chosen appropriately. Hence, based on the edge detection operation with LBPs described in the previous sub-section, we construct the LBPSF as follow:

$$g_{LBP} = 1 - B \tag{5.7}$$

where *B* is the binary image resulting from the Canny edge detector with LBPs.

The function g_{LBP} is made such as it is zero on edges whereas it is equal to one on flat and noisy regions, accordingly, the active contour will keep evolving in flat and noisy regions till it attains the object boundaries (the edges). Replacing the ESF g of the GAC model in a variational formulation by the proposed LBPSF g_{LBP}, the total energy function can be defined as:

$$E(\Phi) = \frac{1}{2}\mu \int_\Omega (|\nabla\Phi - 1)^2 dx + \lambda \int_\Omega g_{LBP}\delta(\Phi)|\nabla\Phi| dx + \nu \int_\Omega g_{LBP} H(-\Phi) dx \tag{5.8}$$

The first term in the right hand side of (5.8) controlled by $\mu > 0$ is the internal energy term that penalizes the deviation of the LSF Φ from a SDF, whereas the last two terms controlled by λ and v form the external energy excerpted from the GAC [20], this energy is defined to drive the motion of the curve toward the object's boundaries. $\delta(.)$ and $H(.)$ are the Dirac function and the Heaviside function, respectively. By minimizing (5.8) with respect of Φ, the steepest descent process is the following gradient flow:

$$\frac{\partial\Phi}{\partial t} = \mu\left[\Delta\Phi - div\left(\frac{\nabla\Phi}{|\nabla\Phi|}\right)\right] + \lambda\,\delta(\Phi) div\left(g_{LBP}\frac{\nabla\Phi}{|\nabla\Phi|}\right) + \nu\delta(\Phi) g_{LBP} \tag{5.9}$$

where Δ and *div(.)* are the laplacien and the divergence operators, respectively.

The method in [54] not only eliminates the need of costly re-initialization, but also allows the use of more general initial LSF rather than a SDF initial function, a binary step function is proposed as an initial LSF defined as in (3.12).

5.3. Results

In this section, in order to validate the performance of the proposed model, we apply and compare it with the gradient based ACM of [20], the global region based ACM of [60] and the local region based ACM proposed in [34] using both synthetic and real gray level images. All models are implemented using Matlab 7.0 in Windows 7; on 3.3 GHz Intel core i3 PC with 4GB of RAM. Unless otherwise specified, the parameters are described in Table 5.1.

This validation and comparison are performed on a set of 10 gray level images consists of: a synthetic image with intensity inhomogeneity, a synthetic image with several intensity levels, a fluorescence microscopic image, two noisy ultrasound images of the left ventricle of a human heart, a magnetic resonance images of the same organ, a cardiac CT image, a liver CT image, a radiographic image of weld defect and a ship in a thermal infrared image, and the results are illustrated in Fig. 5.5 and Fig. 5.6.

Parameters	Description
d	To initialize the LSF, $d > 0$ is a constant.
σ, ρ	Width of the Gaussian kernel in [20], region scale parameter in [34] (determined according to images).
Δt	Time step ([20] and [34]: $\Delta t = 0.1$, [60] our model: $\Delta t = 1$).
μ	Regularization parameter of internal energy (our model: $\mu = 0.04$).
λ, v	Regularization parameters of the curve (our model: $\lambda = 5$, $v = \pm 3$ (-) if initial curve is located inside or (+) if it is outside).
α	Balloon parameter of the GAC [20].
P,R	LBP parameters (number of neighbors and LBP radius ($P = 8$, $R = 1$)).
t_1,t_2	Threshold parameters determined empirically according to images.

Table 5.1: Description of the parameters used in the study.

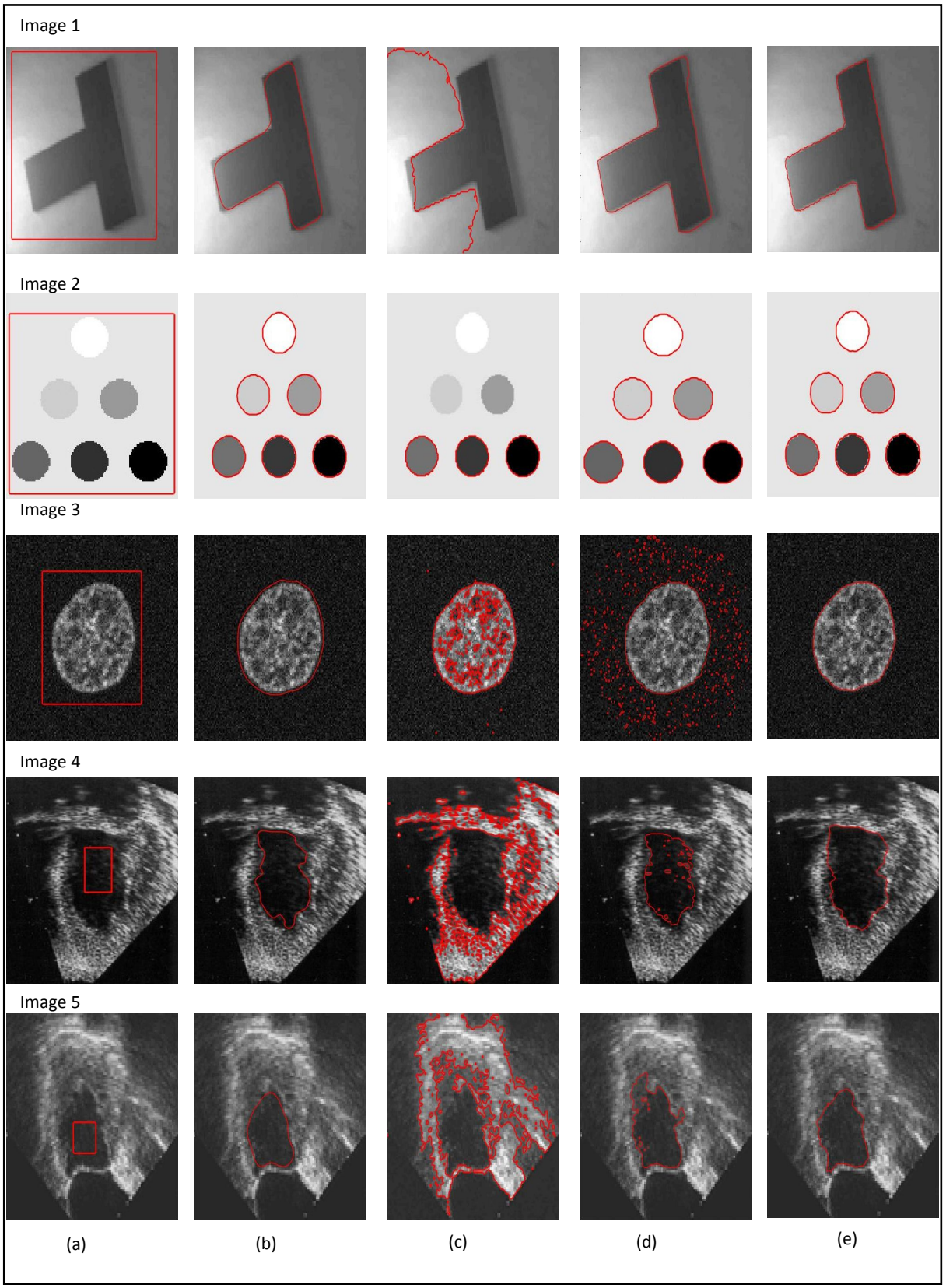

Figure 5.5: Comparison between the different active contour models. (a) Original images with initial contours. Segmentation output of: (b) GAC model [20] ($\sigma = 1.2$ for all images), (c) global region-based model [60], (d) local region based-model [34] (Image 1: $\rho = 6.0$, Images: 2, 3, and 4: $\rho = 3.0$, Image 5: $\rho = 1.5$), and (e) the proposed model.

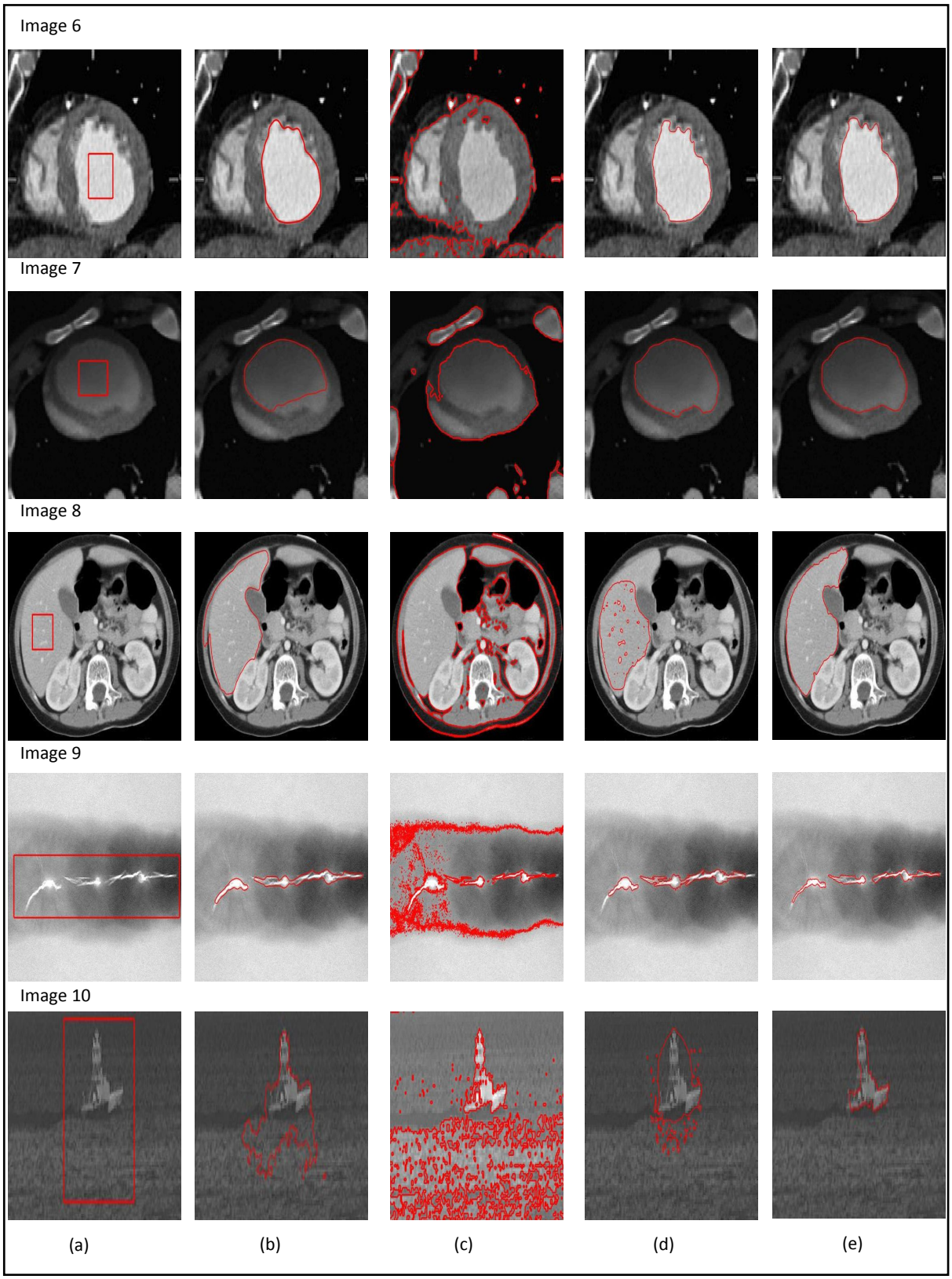

Figure 5.6: Comparison between the different active contour models. (a) Original images with initial contours. Segmentation output of: (b) GAC model [20] ($\sigma = 4$ for image 8, $\sigma = 1.2$ for others), (c) global region-based model [60], (d) local region-based model [34] (Image 6, 7, and 8: $\rho = 3.0$, Image 9: $\rho = 6.0$, Image 10: $\rho = 4.0$), and (e) the proposed model.

From these results, it is clear that the proposed ACM based LBPSF outperforms the other ACMs in term of efficiency (boundary detection).

In particular, Compared the proposed model to the GAC model [20], no smoothing is necessary for the LBPSF, while the ESF deals with the problem that smoothing with big filter size (eq. (2.23)) can suppress important edges and the curve will pass through them (Image 1 and 8), but small filter size may not be sufficient to remove noise and then, the curve will stop evolving before reaching the real object boundaries (Images: 3, 4, 5, 7, 9 and 10).

For more comparison, some visualized LBPSF images of the set are contrasted with the ESF images in Fig. 5.7. Contrary to the ESF, it is clearly seen that the LBPSF can accurately distinguish the object boundaries.

Moreover, Fig. 5.8 shows the line profile plots for both LBPSF and ESF values across the hat area of image 8. Here the noisy and poorly defined liver boundary (edge) along the profile is located at the pixel number “15”; unlike the ESF, the value of the LBPSF is exactly “0” on the edge and “1” in the two regions beside it. The graph shows that LBPSF is a robust indicator of poorly defined or noisy edges.

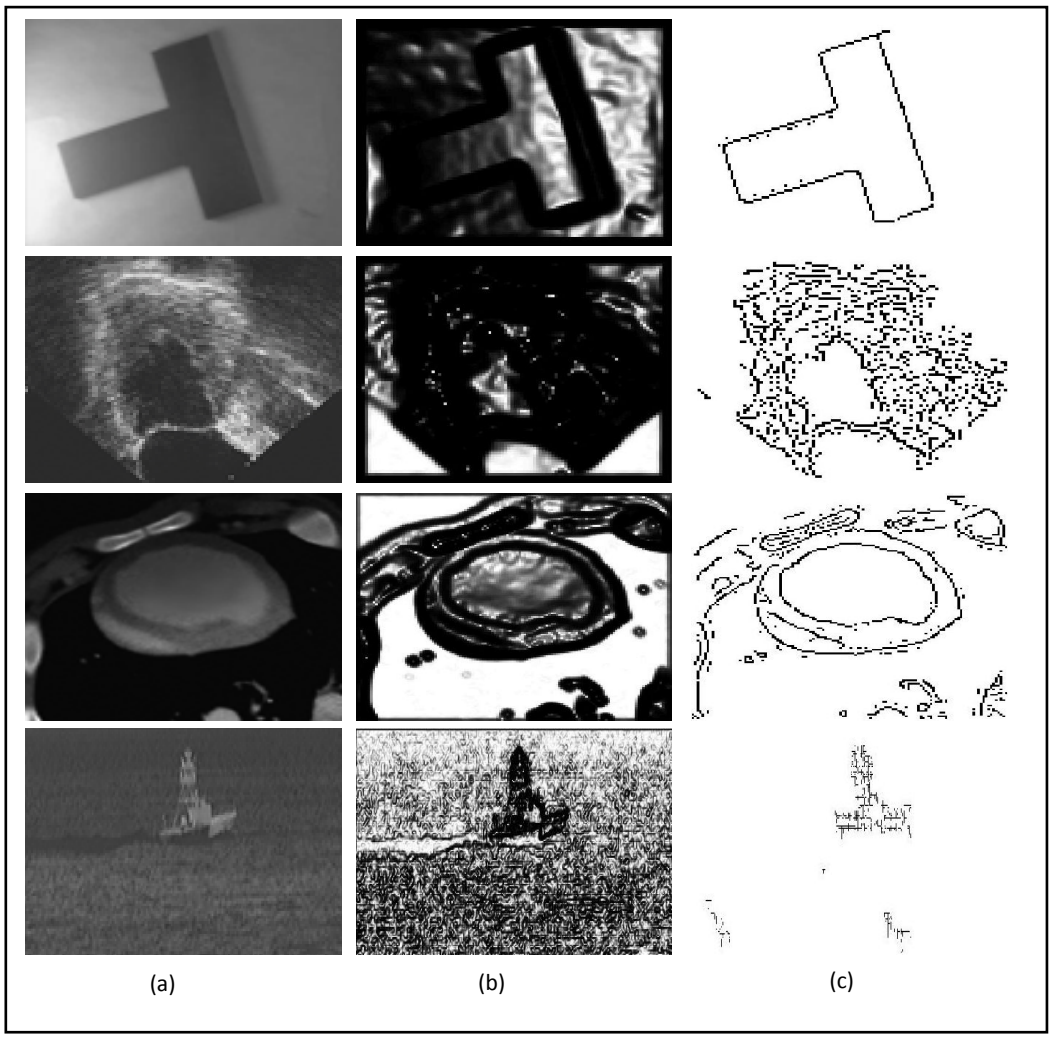

Figure 5.7: Comparison between the ESF and the LBPSF. (a) Original images, (b) the visualized ESF of the original images, and (c) the visualized LBPSF of the original images.

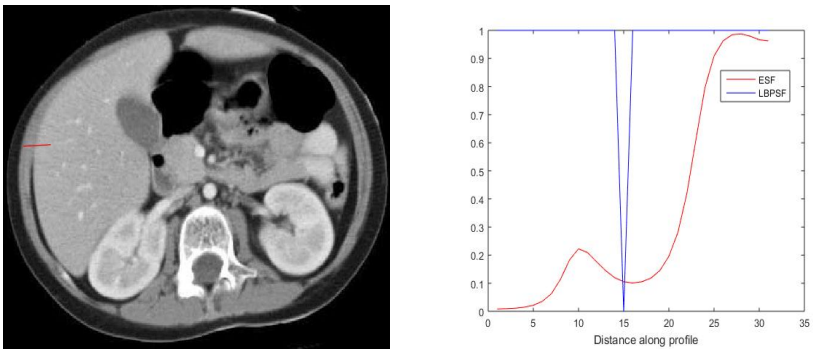

Figure 5.8: Comparison between the ESF and the LBPSF. (a) Original liver CT image, (b) ESF and LBPSF values along a line (red) segment in the original image.

Here the proposed model outperforms the model proposed in [60] since the set of images used requires local segmentation property, and the global region-based ACMs generally suffer from intensity inhomogeneity problem.

Comparing the proposed model to the model proposed in [34] which gives closely similar results to those obtained by our model on images with several intensity levels (Image 2) or with intensity inhomogeneity (Images: 1, 6 and 7), this model seems to be sensitive to noise (Images: 3, 4, 5 and 10) and the segmentation result relies on the size of the region scale parameter (ρ) (Images: 8 and 9).

To show the sensitivity of this model to region scale parameter (ρ), we used images: 3, 6, 7 and 9 with three different sizes of ρ (1.5, 3.0, and 6.0). Fig. 5.9 shows that depending on the image, small value of ρ leads to local segmentation when the intensity inhomogeneity is severe (second and third row) while large value is chosen in noisy and smooth regions (first and last row).

Moreover the Dice coefficient [71] is used to compare and measure the segmentation accuracy. The Dice index $D \in [0,1]$ between the obtained segmentation result R_R and the ground truth R_G is given by: $D(R_R \cap R_G) = \frac{2Area(R_R \cap R_G)}{Area(R_R)+Area(R_R)}$. A higher Dice value (close to 1) indicates better segmentation performance.

From the quantitative performance measure showed in Fig. 5.10 and Table 5.2, we observe that the proposed model yields almost the best segmentation accuracy with an average Dice score of 0.96, compared to 0.34, 0.89 and 0.91 for the models proposed in [60], [20] and [34] respectively.

Computationally, we have not mention computation time in this study since the related methods and the proposed one use different level set strategies (PDE based LSM for the models proposed in [20] and [60] and variational LSM for the model proposed in [34] and our model). More precisely, the number of iterations of the model proposed in [60] ranges from 5 to 7 iterations, while for other models including the proposed one, the range of these values from 200 to 600 iterations over the set of images used.

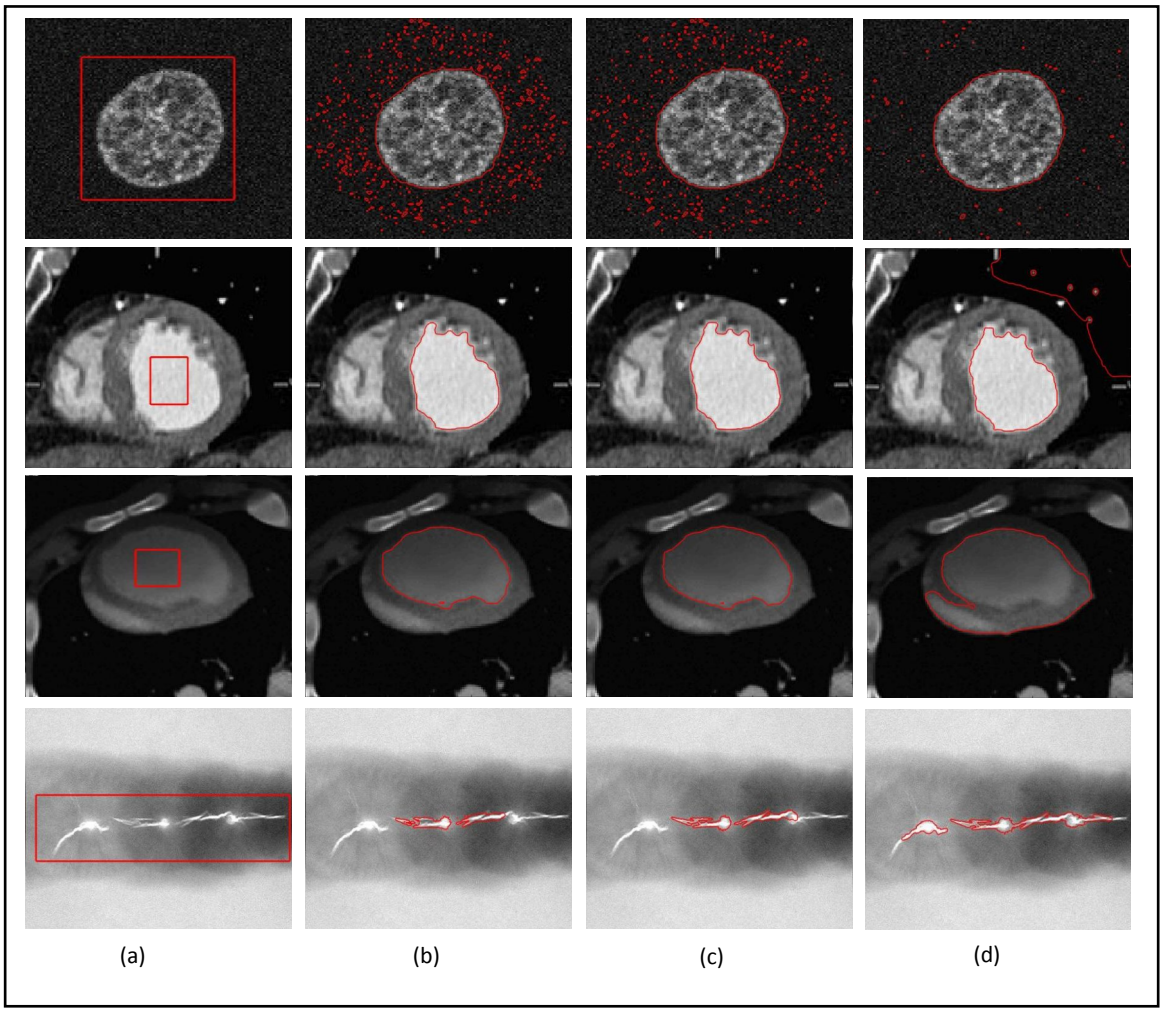

Figure 5.9: Segmentation results by the model of [34]. (a) Original images with initial contours, (b), (c) and (d) are the segmentation results with $\rho = 1.5$, $\rho = 3.0$ and $\rho = 6.0$, respectively.

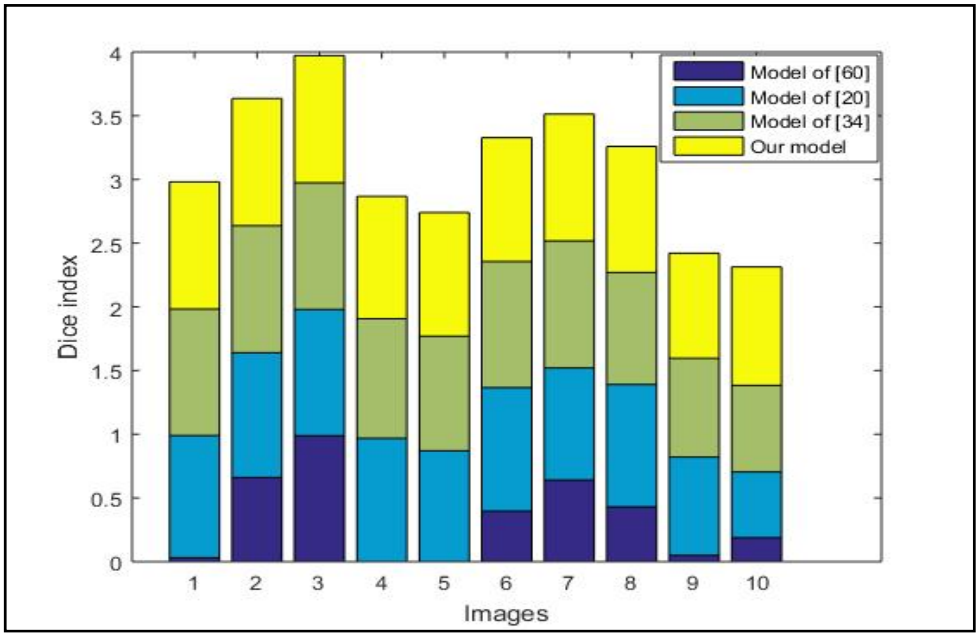

Figure 5.10: Segmentation accuracy as calculated via the Dice index for each model.

Image	D of the model of [60]	D of the model of [20]	D of the model of [34]	D of the proposed model
Image 1	0.03	0.96	0.992	**0.999**
Image 2	0.66	0.98	0.997	**0.999**
Image 3	0.988	0.992	0.997	**0.999**
Image 4	0	**0.968**	0.939	0.961
Image 5	0	0.87	0.9	**0.97**
Image 6	0.4	0.97	**0.99**	0.972
Image 7	0.64	0.88	**0.997**	0.996
Image 8	0.43	0.96	0.88	**0.961**
Image 9	0.05	0.77	0.776	**0.82**
Image 10	0.19	0.52	0.68	**0.93**

Table 5.2: Values of the Dice index (D) of the different models used in the study (Fig. 5.5 and Fig. 5.6).

5.4. Conclusion

In this Chapter, a robust and efficient active contour model has been proposed by combining the local binary pattern stopping function (LBPSF) with the GAC model in a variational level set formulation. Comparatively to edge stopping function (ESF), the LBPSF accurately distinguishes the noisy and poorly defined boundaries or edges. Experimental results and quantitative analysis showed that our method outperforms the related methods in terms of boundary detection and segmentation accuracy.

Conclusion and future work

In this thesis, we first provided a literature review behind ACMs to show various types based on curve representation (parametric and geometric ACMs), the level set strategy (PDE and variational) and the image information used (Edge-based models and region-based models) to deal with object detection or segmentation problem. However, a number of models have been presented to deal with segmentation problems met with some state of art ACMs. In this final Chapter, the results from previous Chapters are summarized and additional research is proposed that can extend the efforts described in the previous three Chapters of this thesis.

6.1. Summary of contributions

In Chapter 3, in order to raise the performance of ACM, we proposed a hybrid ACM embeds both edge and region information within a variational level set framework. The combination of the edge and region information gave the hybrid model their advantages; i.e. bidirectional motion of the curve, robustness against noise and detecting discreet edges as advantages of using region information, and detecting objects with high variation in gradient at boundaries even in the presence of intensity inhomogeneity for edge information. In addition, the variational level set formulation uses a penalizing term that forces the LSF to be close to SDF to eliminate costly re-initialization and speed up the motion of the curve. Experimental results on both synthetic and real images show that the hybrid model works better than traditional edge-based and region-based models.

Chapter 4 gave several possible solutions to improve the robustness of local region-based ACM, where a region-based ACM based on local signed pressure Force (LSPF) function has been proposed. The LSPF considers local information which modulates the signs of the pressure force inside and outside the curve locally, which helps the model to work well with intensity inhomogeneity. The proposed model uses a simple and efficient level set updating formulation by using directly current LSF instead of its curvature approximation and a simple morphological opening and closing process to smooth the LSF which make it less sensitive to noise and to the initialization of the curve compared with other ACMs.

Eventually, with the aim of developing an edge-based ACM that is at the same time effective and robust in handling images with intensity inhomogeneity, we have proposed in Chapter 5 an edge-based ACM guided with local binary pattern stopping function (LBPSF). The main motivation is to improve the robustness of ESF against noise and poorly defined

boundaries by introducing a new stopping function based on texture analysis with LBP textons. Indeed, LBP textons are used to classify image regions into noisy, homogeneous and edge regions which helps to construct LBPSF such as it is zero on edges whereas it is equal to one on flat and noisy regions. Comparatively to ESF, the LBPSF accurately distinguishes the noisy and poorly defined boundaries.

6.2. Recommended future work

There are still several issues that need to be further developed in the future.

All methods that have been proposed are defined and tested just on gray value images, opening a possibility to extend them to color image.

In Chapter 3, the competition between edge and region information is made based on a weighting function taking into account gradient information, and we may add other information such as the degree of inhomogeneity based on local image contrast.

The size of the locality in local region-based ACMs affects the segmentation results, developing a method adapting this parameter may raise the performance of local models.

Finally, for the ACM based on LBP proposed in Chapter 5, future work will be devoted to improve its performance by developing an automatic method to define threshold parameter in the hysteresis thresholding step.

Functional minimization

A functional is a mapping E which assigns to each element of a vector-space (to each function u) an element from the underlying field (a number).

Let's consider a particular class of functionals, that we call it a canonical class:

$$E(u) = \int \mathcal{L}(u, \acute{u})dx \tag{A.1}$$

Where $\acute{u} = \frac{du}{dx}$ is the derivative of the function u. (In physics $\mathcal{L}$ is called the Lagrange density).

We want to treat this class of cost functions (functionals) because the theory we will develop should be independent of what exact cost function we use; it is some quantity evaluated for each pixel and aggregated over all pixels, and this quantity in this example will depend on u and its derivative at location x, but the theory can be generalized for high order derivatives (second, third…).

Just as with real-valued functions defined on $\mathbb{R}^n$ the necessary condition for extremality of the functional E states that the derivative with respect to u must be 0.

Yet how does one define and compute the derivative of a functional $E(u)$ with respect to the function u?

The Gâteaux Derivative:

There are several ways to introduce functional derivatives. The following definition goes back to works of the French mathematician R. Gâteaux which were published posthumously in 1919.

The Gâteaux derivative extends the concept of directional derivative to infinite-dimensional spaces. The derivative of the functional $E(u)$ in direction $h(x)$ is defined as:

$$\left.\frac{dE(u)}{du}\right|_h = \lim_{\epsilon \to 0} \frac{E(u+\epsilon\, h) - E(u)}{\epsilon} \tag{A.2}$$

As in finite dimensions, this directional derivative can be interpreted as the projection of the functional gradient on the respective direction. We can therefore write:

$$\left.\frac{dE(u)}{du}\right|_h = \langle \frac{dE(u)}{du}, h \rangle = \int \frac{dE(u)}{du}(x)h(x)dx \tag{A.3}$$

For functionals of the canonical form: $E(u) = \int \mathcal{L}(u, \grave{u})dx$ the Gâteaux derivative is given by:

$$\left.\frac{dE(u)}{du}\right|_h = \lim_{\epsilon\to 0}\frac{1}{\epsilon}E(u+\epsilon\, h) - E(u)$$

$$= \lim_{\epsilon\to 0}\frac{1}{\epsilon}\int (\mathcal{L}\big(u+\epsilon h, \acute{u}+\epsilon\acute{h}\big) - \mathcal{L}(u,\acute{u}))dx$$

$$= \lim_{\epsilon\to 0}\frac{1}{\epsilon}\int (\left(\mathcal{L}(u,\acute{u}) + \frac{\partial\mathcal{L}}{\partial u}\epsilon h + \frac{\partial\mathcal{L}}{\partial\acute{u}}\epsilon\acute{h} + o(\epsilon^2)\right) - \mathcal{L}(u,\acute{u}))dx$$

$$= \int (\frac{\partial\mathcal{L}}{\partial u}h + \frac{\partial\mathcal{L}}{\partial\acute{u}}\acute{h})\,dx$$

$$= \int (\frac{\partial\mathcal{L}}{\partial u}h - \frac{d}{dx}\frac{\partial\mathcal{L}}{\partial\acute{u}}h)\,dx \quad (partial\ int, h = 0\ on\ boundary)$$

$$= \int \underbrace{(\frac{\partial\mathcal{L}}{\partial u} - \frac{d}{dx}\frac{\partial\mathcal{L}}{\partial\acute{u}})}_{\frac{dE}{du}} h(x)dx$$

Euler-Lagrange equation:

Thus the derivative of the functional $E(u)$ in direction h is:

$$\left.\frac{dE(u)}{du}\right|_h = \int \underbrace{(\frac{\partial\mathcal{L}}{\partial u} - \frac{d}{dx}\frac{\partial\mathcal{L}}{\partial\acute{u}})}_{\frac{dE}{du}} h(x)dx \tag{A.4}$$

As a necessary condition for minimality of the functional $E(u)$ the variation of E in any direction $h(x)$must vanish. Therefore at the extremum we have:

$$\frac{dE}{du} = \frac{\partial\mathcal{L}}{\partial u} - \frac{d}{dx}\frac{\partial\mathcal{L}}{\partial\acute{u}} = 0 \tag{A.5}$$

This condition is called the Euler-Lagrange equation.

The Euler-Lagrange equation is a differential equation which forms the necessary condition for minimality.

The central idea of variational methods is to compute solutions to the respective Euler-Lagrange equation.

For general (non-quadratic) energies, one can start with an initial guess $u_0(x)$ of the solution and iteratively improve the solution. Such methods are called descent methods.

How can one iteratively improve a given solution?

Gradient Descent:

Gradient descent or steepest descent is a particular descent method where in each iteration one chooses the direction in which the energy decreases most. The direction of steepest descent is given by the negative energy gradient.

To minimize a real-valued function $f: \mathbb{R}^n \to \mathbb{R}$, the gradient descent for $f(u)$ is defined by the differential equation:

$$\begin{cases} u(0) = u_0 \\ \frac{du}{dt} = -\frac{df}{du}(u) \end{cases} \tag{A.6}$$

Discretization: $u_{t+1} = u_t - \epsilon \frac{df}{du}(u_t), \qquad t = 0,1,2, \dots$

For minimizing functionals $E(u)$, the gradient descent is done analogously. For the functional $E(u) = \int \mathcal{L}(u, \acute{u}) dx$, the gradient is given by:

$$\frac{dE}{du} = \frac{\partial \mathcal{L}}{\partial u} - \frac{d}{dx}\frac{\partial \mathcal{L}}{\partial \acute{u}} \tag{A.7}$$

Therefore the gradient descent is given by:

$$\begin{cases} u(x,0) = u_0(x) \\ \frac{\partial u(x,t)}{\partial t} = -\frac{dE}{du} = -\frac{\partial \mathcal{L}}{\partial u} + \frac{\partial}{\partial x}\frac{d\mathcal{L}}{d\acute{u}} \end{cases} \tag{A.8}$$

If the gradient descent converges, i.e. $\partial_t u = -\frac{dE}{du} = 0$, then we have found a solution to the Euler-Lagrange equation.

Addendum: Boundary Conditions:

When deriving the Euler-Lagrange equations we only considered perturbations $h(x)$ which are 0 on the boundary. Without this assumption, Gâteaux's directional derivative is:

$$\left.\frac{dE(u)}{du}\right|_h = \cdots = \int_a^b \left(\frac{\partial \mathcal{L}}{\partial u} h + \frac{\partial}{\partial x}\frac{d\mathcal{L}}{d\acute{u}} \acute{h}\right) dx$$

$$= \int_a^b \left(\frac{\partial \mathcal{L}}{\partial u} h - \frac{d}{dx}\frac{\partial \mathcal{L}}{\partial \acute{u}} h\right) dx + \left(\frac{\partial \mathcal{L}}{\partial \acute{u}} h(x)\right)_a^b$$

$$\left.\frac{dE(u)}{du}\right|_h = \int_a^b \left(\frac{\partial \mathcal{L}}{\partial u} - \frac{d}{dx}\frac{\partial \mathcal{L}}{\partial \acute{u}}\right) h(x)dx + \left(\frac{\partial \mathcal{L}}{\partial \acute{u}} h(x)\right)_a^b = 0$$

$$\Rightarrow \begin{cases} 1)\ \frac{dE}{du} = \frac{\partial \mathcal{L}}{\partial u} - \frac{d}{dx}\frac{\partial \mathcal{L}}{\partial \acute{u}} = 0 \\ 2)\ \left(\frac{\partial \mathcal{L}}{\partial \acute{u}} h(x)\right)_a^b = 0 \end{cases} \tag{A.9}$$

Depending on the application one can distinguish two kinds of boundary conditions:

- Dirichlet boundary conditions: the function $u(x)$ is fixed on the boundary ($u_r(x)$), i.e. $h(x) = 0$ on the boundary. One only considers variations of $u(x)$ inside the domain:

$$\begin{cases} \frac{dE}{du} = \frac{\partial \mathcal{L}}{\partial u} - \frac{d}{dx}\frac{\partial \mathcal{L}}{\partial \acute{u}} = 0 \\ u(x)|_{boundary} = u_r(x) \end{cases} \tag{A.10}$$

- Neumann boundary conditions: one additionally allows for variations of $u(x)$ on the boundary:

$$\begin{cases} \frac{dE}{du} = \frac{\partial \mathcal{L}}{\partial u} - \frac{d}{dx}\frac{\partial \mathcal{L}}{\partial \acute{u}} = 0 \\ \left.\frac{\partial \mathcal{L}}{\partial \acute{u}}\right|_{boundary} = 0 \end{cases} \tag{A.11}$$

Implementation for the piecewise constant M-S functional (two regions case)

Unfortunately, the M-S functional in its original formulation is not in a canonical form $E(u) = \mathcal{L}(u, \dot{u}, \ddot{u})$. Since the variable of interest (the boundary C) appears in the integrand.

Following green's theorem [40], we will derive the Euler Lagrange equation:

Assume we are given energy of the form

$$E(C) = \int_{int(C)} f(x,y)\, dxdy \tag{B.1}$$

Where $int(C)$ denotes the region inside a curve C. Let $C: [0,1] \to \mathbb{R}^2$ be a parametric closed curve, with $C(s) = (x(s), y(s))$.

Green's theorem: For a victor field of the form $\vec{V} = \big(a(x,y), b(x,y)\big) \epsilon\, \mathbb{R}^2$ and a closed boundary $C \subset \Omega$, we have:

$$\int_{int(C)} (\nabla \times \vec{V}) dx = \int_C \vec{V}\, dS \tag{B.2}$$

Where the rotation of $\vec{V}$ is defined as $\nabla \times \vec{V} \equiv \partial_x b - \partial_y a$, thus:

$$\int_{int(C)} \big(b_x - a_y\big) dxdy = \int_C a\, dx + b\, dy \tag{B.3}$$

Closing a vector field $\vec{V}$ such that $f = \big(b_x - a_y\big)$, we can rewrite the energy in the canonical form:

$$E(C) = \int_{int(C)} f\, dxdy = \int_C a\, dx + b\, dy = \int_0^1 (a\dot{x} + b\dot{y}) dS \equiv \int_0^1 \mathcal{L}(x, \dot{x}, y, \dot{y}) dS \tag{B.4}$$

Where $\dot{x} \equiv \frac{dx(S)}{dS}$ and $\dot{y} \equiv \frac{dy(S)}{dS}$

The functional $E(C)$ is equal to an integral along the curve C and we can compute the functional derivative with respect to $C(S) = (x(S), y(S))$:

$$\left.\begin{aligned}\frac{\partial \mathcal{L}}{\partial x}-\frac{d}{dS}\frac{\partial \mathcal{L}}{\partial \dot{x}}=\frac{\partial a}{\partial x}\dot{x}+\frac{\partial b}{\partial x}\dot{y}-\frac{d}{dS}a=\left(\frac{\partial b}{\partial x}-\frac{\partial a}{\partial y}\right)\dot{y}=f\dot{y}\\ \frac{\partial \mathcal{L}}{\partial y}-\frac{d}{dS}\frac{\partial \mathcal{L}}{\partial \dot{y}}=\frac{\partial a}{\partial y}\dot{x}+\frac{\partial b}{\partial y}\dot{y}-\frac{d}{dS}b=\left(-\frac{\partial b}{\partial x}+\frac{\partial a}{\partial y}\right)\dot{x}=-f\dot{x}\end{aligned}\right\}\ \frac{\partial \mathcal{L}}{\partial C}-\frac{d}{dS}\frac{\partial \mathcal{L}}{\partial \dot{C}} \tag{B.5}$$

In summary we obtain the simple functional gradient

$$\frac{dE}{dC}=\frac{\partial \mathcal{L}}{\partial C}-\frac{d}{dS}\frac{\partial \mathcal{L}}{\partial \dot{C}}=f(x,y)\begin{pmatrix}\dot{y}\\-\dot{x}\end{pmatrix}=f\,\overrightarrow{n_C} \tag{B.6}$$

Where $\overrightarrow{n_C}$ is the outer normal for the piecewise constant M-S functional with two regions (without boundary length term):

$$E(C)=\int_{int}(I(x)-u_{int})^2d^2x+\int_{ext(C)}(I(x)-u_{ext})^2d^2x \tag{B.7}$$

So the functional derivative is given by:

$$\frac{dE}{dC}=((I(x)-u_{int})^2-(I(x)-u_{ext})^2)\,\overrightarrow{n_C} \tag{B.8}$$

For the two regions piecewise constant M-S with length regularity, we get:

$$E(C)=\int_{int(C)}(I(x)-u_{int})^2d^2x+\int_{ext(C)}(I(x)-u_{ext})^2d^2x+v|C| \tag{B.9}$$

And the gradient decent reads:

$$\frac{\partial C(S,t)}{\partial t}=-\frac{dE(C)}{dC}=((I-u_{ext})^2-(I-u_{int})^2-\ vk_C)\,\overrightarrow{n_C} \tag{B.10}$$

Where k_C denotes the local curvature of the curve C.

This means that additional to separating bright and dark areas, the evolution aims at suppressing large curvature of the curve.

Minimization of the hybrid ACM energy

The energy functional of the proposed hybrid ACM is given by:

$$E(\Phi) = \frac{1}{2}\mu \int_{\Omega} (|\nabla\Phi| - 1)^2 dx + \int_{\Omega} g|\nabla H(\Phi)| dx + \int_{\Omega} gF\, H(-\Phi) dx \quad \text{(C.1)}$$

So we can re-write the functional in the following form

$$\begin{aligned} \mathcal{L} &= \mathcal{L}_1 + \mathcal{L}_2 + \mathcal{L}_3 \\ &= \frac{1}{2}\mu(|\nabla\Phi| - 1) + g|\nabla H(\Phi)| + gFH(-\Phi) \end{aligned} \quad \text{(C.2)}$$

We can compute:

$$\frac{\partial E}{\partial \Phi} = \frac{\partial \mathcal{L}}{\partial \Phi} - div\left(\frac{\partial \mathcal{L}}{\partial \nabla \Phi}\right) = \sum_{i=1}^{i=3}\left(\frac{\partial \mathcal{L}_i}{\partial \Phi} - div\left(\frac{\partial \mathcal{L}_i}{\partial \nabla \Phi}\right)\right) \quad \text{(C.3)}$$

So

- $\frac{\partial \mathcal{L}_1}{\partial \nabla \Phi} = \mu(|\nabla\Phi| - 1).\frac{\nabla\Phi}{|\nabla\Phi|}$

  $= \mu(\nabla\Phi - \frac{\nabla\Phi}{|\nabla\Phi|})$

  and

  $\frac{\partial \mathcal{L}_1}{\partial \Phi} = 0$

- $\mathcal{L}_2 = g|\nabla H(\Phi)| = g\delta(\Phi)|\nabla\Phi|$

  $\frac{\partial \mathcal{L}_2}{\partial \nabla \Phi} = g\delta(\Phi)\frac{\nabla\Phi}{|\nabla\Phi|}$

  and

  $\frac{\partial \mathcal{L}_2}{\partial \Phi} = \acute{\delta}(\Phi)\mathrm{g}|\nabla\Phi|$

- $\frac{\partial \mathcal{L}_3}{\partial \Phi} = -gF(\delta(\Phi))$

  and

  $\frac{\partial \mathcal{L}_3}{\partial \nabla \Phi} = 0$

Combining all results in (C.3), gives:

$$\frac{\partial E}{\partial \Phi} = -\mu div\left[\nabla\Phi - \frac{\nabla\Phi}{|\nabla\Phi|}\right] + \acute{\delta}(\Phi)g|\nabla\Phi| - div\left(g.\delta(\Phi)\frac{\nabla\Phi}{|\nabla\Phi|}\right) - gF\delta(\Phi) \quad \text{(C.4)}$$

Further evaluating of $div(g\ \delta(\Phi)\frac{\nabla\Phi}{|\nabla\Phi|})$ gives:

$$div(g\ \delta(\Phi)\frac{\nabla\Phi}{|\nabla\Phi|} = \frac{d}{dx}(\delta(\Phi)g\frac{\Phi_x}{|\nabla\Phi|}) + \frac{d}{dy}(\delta(\Phi)g\frac{\Phi_y}{|\nabla\Phi|})$$
$$= \frac{d}{dx}\delta(\Phi)g\frac{\Phi_x}{|\nabla\Phi|} + \left(\frac{d}{dx}g\frac{\Phi_x}{|\nabla\Phi|}\right)\delta(\Phi) + \frac{d}{dy}\delta(\Phi)g\frac{\Phi_y}{|\nabla\Phi|} + \left(\frac{d}{dy}g\frac{\Phi_y}{|\nabla\Phi|}\right)\delta(\Phi)$$
$$= \delta(\Phi)\Phi_x g\frac{\Phi_x}{|\nabla\Phi|} + \left(\frac{d}{dx}g\frac{\Phi_x}{|\nabla\Phi|}\right)\delta(\Phi) + \delta(\Phi)\Phi_y g\frac{\Phi_y}{|\nabla\Phi|} + \left(\frac{d}{dy}g\frac{\Phi_y}{|\nabla\Phi|}\right)\delta(\Phi)$$
$$= \delta(\Phi)div\left(g\frac{\nabla\Phi}{|\nabla\Phi|}\right) + \acute{\delta}(\Phi)g\nabla\Phi\frac{\nabla\Phi}{|\nabla\Phi|}$$
$$= \delta(\Phi)div\left(g\frac{\nabla\Phi}{|\nabla\Phi|}\right) + \acute{\delta}(\Phi)g|\nabla\Phi|$$

So the Euler Lagrange equation (C.4) becomes

$$\frac{\partial E}{\partial \Phi} = -\mu\left[\nabla\Phi - div\frac{\nabla\Phi}{|\nabla\Phi|}\right] - \delta(\Phi)div\left(g\frac{\nabla\Phi}{|\nabla\Phi|}\right) - gF\delta(\Phi) \quad \text{(C.5)}$$

Therefore the gradient descent of (C.5) is:

$$\frac{\partial \Phi}{\partial t} = -\frac{\partial E}{\partial \Phi} = \mu(\nabla\Phi + div\frac{\nabla\Phi}{|\nabla\Phi|}) + \delta(\Phi)div\left(g\frac{\nabla\Phi}{|\nabla\Phi|}\right) + gF\delta(\Phi) \quad \text{(C.6)}$$

with $div\left(g\frac{\nabla\Phi}{|\nabla\Phi|}\right) = g\ div\left(\frac{\nabla\Phi}{|\nabla\Phi|}\right) + \nabla g\ |\nabla\Phi|$

So, (C.6) becomes:

$$\frac{\partial \Phi}{\partial t} = -\frac{\partial E}{\partial \Phi} = \mu(\nabla\Phi + div\frac{\nabla\Phi}{|\nabla\Phi|}) + \delta(\Phi)(g\ div\left(\frac{\nabla\Phi}{|\nabla\Phi|}\right) + \nabla g\ |\nabla\Phi|) + gF\delta(\Phi) \quad \text{(C.7)}$$

Bibliography

[1] Qing Yang. (2013). Ultrasound image segmentation using local statistics with an adaptive scale selection. Computer Science [cs]. Université de Technologie de Compiègne.

[2] Cremers, D. (2002). Statistical shape knowledge in variational image segmentation (Doctoral dissertation, Universität Mannheim).

[3] Abdelsamea, M. (2015). Regional Active Contours based on Variational level sets and Machine Learning for Image Segmentation. arXiv preprint arXiv:1511.00111.

[4] Otsu, N. (1975). A threshold selection method from gray-level histograms. *Automatica*, *11*(285-296), 23-27.

[5] Abdelsamea, M. M., Gnecco, G., & Gaber, M. M. (2015). A SOM-based Chan–Vese model for unsupervised image segmentation. Soft Computing, 1-21.

[6] Sobel, I., & Feldman, G. (1968). A 3x3 isotropic gradient operator for image processing. *a talk at the Stanford Artificial Project in*, 271-272.

[7] Prewitt, J. M. (1970). Object enhancement and extraction. *Picture processing and Psychopictorics*, *10*(1), 15-19.

[8] Raut, S. A., Raghuwanshi, M., Dharaskar, R., & Raut, A. (2009, January). Image segmentation–a state-of-art survey for prediction. In *Advanced Computer Control, 2009. ICACC'09. International Conference on* (pp. 420-424). IEEE.

[9] Canny, J. (1986). A computational approach to edge detection. *IEEE Transactions on pattern analysis and machine intelligence*, (6), 679-698.

[10] Shariat, Farnaz. (2009). "Object Segmentation Using Active Contours: A Level Set Approach". Electronic Theses and Dissertations. Paper 336.

[11] Brice, C. R., & Fennema, C. L. (1970). Scene analysis using regions. *Artificial intelligence*, *1*(3), 205-226.

[12] Adams, R., & Bischof, L. (1994). Seeded region growing. *IEEE Transactions on pattern analysis and machine intelligence*, *16*(6), 641-647.

[13] Abdelsamea, M. M., Gnecco, G., Gaber, M. M., & Elyan, E. (2015). On the relationship between variational level set-based and som-based active contours. *Computational intelligence and neuroscience*, *2015*, 34.

[14] Kass, M., Witkin, A., & Terzopoulos, D. (1988). Snakes: Active contour models. *International journal of computer vision*, *1*(4), 321-331.

[15] Azizi, A., & Elkourd, K. (2016). Fast Region-based Active Contour Model Driven by Local Signed Pressure Force. *ELCVIA Electronic Letters on Computer Vision and Image Analysis*, *15*(1), 1-13.

[16] Cohen, L. D. (1991). On active contour models and balloons. *CVGIP: Image understanding*, *53*(2), 211-218.

[17] Xu, C., & Prince, J. L. (1998). Snakes, shapes, and gradient vector flow. IEEE Transactions on image processing, 7(3), 359-369.

[18] Wu, Y., Wang, Y., & Jia, Y. (2013). Adaptive diffusion flow active contours for image segmentation. Computer Vision and Image Understanding, 117(10), 1421-1435.

[19] Caselles, V., Catté, F., Coll, T., & Dibos, F. (1993). A geometric model for active contours in image processing. Numerische mathematik, 66(1), 1-31.

[20] Caselles, V., Kimmel, R., & Sapiro, G. (1997). Geodesic active contours. International journal of computer vision, 22(1), 61-79.

[21] Malladi, R., Sethian, J. A., & Vemuri, B. C. (1995). Shape modeling with front propagation: A level set approach. IEEE transactions on pattern analysis and machine intelligence, 17(2), 158-175.

[22] Yezzi, A., Kichenassamy, S., Kumar, A., Olver, P., & Tannenbaum, A. (1997). A geometric snake model for segmentation of medical imagery. IEEE Transactions on medical imaging, 16(2), 199-209.

[23] Li, C., Xu, C., Gui, C., & Fox, M. D. (2010). Distance regularized level set evolution and its application to image segmentation. IEEE transactions on image processing, 19(12), 3243-3254.

[24] Chan, T. F., & Vese, L. A. (2001). Active contours without edges. IEEE Transactions on image processing, 10(2), 266-277.

[25] Kimia, B. B., Tannenbaum, A. R., & Zucker, S. W. (1995). Shapes, shocks, and deformations I: the components of two-dimensional shape and the reaction-diffusion space. International journal of computer vision, 15(3), 189-224.

[26] Osher, S., & Sethian, J. A. (1988). Fronts propagating with curvature-dependent speed: algorithms based on Hamilton-Jacobi formulations. Journal of computational physics, 79(1), 12-49.

[27] Ksantini, R., Boufama, B., & Memar, S. (2013). A new efficient active contour model without local initializations for salient object detection. EURASIP Journal on Image and Video Processing, 2013(1), 1-13.

[28] Liu, T., Xu, H., Jin, W., Liu, Z., Zhao, Y., & Tian, W. (2014). Medical image segmentation based on a hybrid region-based active contour model. *Computational and mathematical methods in medicine*, *2014*.

[29] Lankton, S., & Tannenbaum, A. (2008). Localizing region-based active contours. IEEE transactions on image processing, 17(11), 2029-2039.

[30] Altarawneh, N. M., & Regan, B. (2014). A novel global threshold-based active contour model. *presented at the Second International Conference on Signal, Image Processing and Pattren Recognition (SIPP)*, Sydney.

[31] Li, C., Kao, C. Y., Gore, J. C., & Ding, Z. (2007, June). Implicit active contours driven by local binary fitting energy. In 2007 IEEE Conference on Computer Vision and Pattern Recognition (pp. 1-7). IEEE.

[32] Liu, S., & Peng, Y. (2012). A local region-based Chan–Vese model for image segmentation. Pattern Recognition, 45(7), 2769-2779.

[33] Li, C., Huang, R., Ding, Z., Gatenby, J. C., Metaxas, D. N., & Gore, J. C. (2011). A level set method for image segmentation in the presence of intensity inhomogeneities with application to MRI. IEEE Transactions on Image Processing, 20(7), 2007-2016.

[34] Zhang, K., Zhang, L., Lam, K. M., & Zhang, D. (2016). A level set approach to image segmentation with intensity inhomogeneity. IEEE transactions on cybernetics, 46(2), 546-557.

[35] Wassima Ait Fares. (2013). Détection et suivi d'objets par vision fondés sur segmentation par contour actif base region. Automatique/ Robotique. Université Paul Sabatier – Toulous III.

[36] Cohen, L. D., & Cohen, I. (1993). Finite-element methods for active contour models and balloons for 2-D and 3-D images. IEEE Transactions on Pattern Analysis and machine intelligence, 15(11), 1131-1147.

[37] Park, H. K., & Chung, M. J. (2002). External force of snake: virtual electric field. *Electronics Letters*, *38*(24), 1500-1502.

[38] Li, B., & Acton, S. T. (2007). Active contour external force using vector field convolution for image segmentation. *IEEE transactions on image processing*, *16*(8), 2096-2106.

[39] Mumford, D., & Shah, J. (1989). Optimal approximations by piecewise smooth functions and associated variational problems. *Communications on pure and applied mathematics*, *42*(5), 577-685.

[40] Zhu, S. C., & Yuille, A. (1996). Region competition: Unifying snakes, region growing, and Bayes/MDL for multiband image segmentation. *IEEE transactions on pattern analysis and machine intelligence*, *18*(9), 884-900.

[41] Yezzi, A., Soatto, S., Tsai, A., & Willsky, A. (2003). The Mumford-Shah functional: From segmentation to stereo. *IMA VOLUMES IN MATHEMATICS AND ITS APPLICATIONS*, *133*, 125-148.

[42] Cremers, D., Tischhäuser, F., Weickert, J., & Schnörr, C. (2002). Diffusion snakes: Introducing statistical shape knowledge into the Mumford-Shah functional. *International journal of computer vision*, *50*(3), 295-313.

[43] McInerney, T., & Terzopoulos, D. (2000). T-snakes: Topology adaptive snakes. *Medical image analysis*, *4*(2), 73-91.

[44] Delingette, H., & Montagnat, J. (2001). Shape and topology constraints on parametric active contours. *Computer Vision and Image Understanding*, *83*(2), 140-171.

[45] Li, C., Liu, J., & Fox, M. D. (2005, June). Segmentation of edge preserving gradient vector flow: an approach toward automatically initializing and splitting of snakes. In *2005 IEEE Computer Society Conference on Computer Vision and Pattern Recognition (CVPR'05)* (Vol. 1, pp. 162-167). IEEE.

[46] Abdallah, A., & Kaouther, E. (2015, November). A Hybrid Active Contour without Re-initialization. In *Proceedings of the International Conference on Intelligent Information Processing, Security and Advanced Communication* (p. 45). ACM.

[47] Dervieux, A., & Thomasset, F. (1980). A finite element method for the simulation of a Rayleigh-Taylor instability. In *Approximation methods for Navier-Stokes problems* (pp. 145-158). Springer Berlin Heidelberg.

[48] Zhang, K., Zhang, L., Song, H., & Zhang, D. (2013). Reinitialization-free level set evolution via reaction diffusion. *IEEE Transactions on Image Processing*, *22*(1), 258-271.

[49] Wang, L., He, L., Mishra, A., & Li, C. (2009). Active contours driven by local Gaussian distribution fitting energy. *Signal Processing*, *89*(12), 2435-2447.

[50] Wu, B., & Yang, Y. (2012). Local-and global-statistics-based active contour model for image segmentation. *Mathematical Problems in Engineering*, *2012*.

[51] Wang, L., Li, C., Sun, Q., Xia, D., & Kao, C. Y. (2009). Active contours driven by local and global intensity fitting energy with application to brain MR image segmentation. *Computerized Medical Imaging and Graphics*, *33*(7), 520-531.

[52] Mahore, N. M., Mante, R. V., & Chatur, P. N. (2014). Approach for MR Image Segmentation and Bias Correction. *International Journal of Advanced Electronics and Communication Systems*.

[53] Goldenberg, R., Kimmel, R., Rivlin, E., & Rudzsky, M. (2001). Fast geodesic active contours. *IEEE Transactions on Image Processing*, *10*(10), 1467-1475.

[54] Li, C., Xu, C., Gui, C., & Fox, M. D. (2005, June). Level set evolution without re-initialization: a new variational formulation. In *2005 IEEE Computer Society Conference on Computer Vision and Pattern Recognition (CVPR'05)* (Vol. 1, pp. 430-436). IEEE.

[55] Chen, L., Zhou, Y., Wang, Y., & Yang, J. (2006). GACV: geodesic-aided C–V method. *Pattern Recognition*, *39*(7), 1391-1395.

[56] Mulder, W., Osher, S., & Sethian, J. A. (1992). Computing interface motion in compressible gas dynamics. *Journal of Computational Physics*, *100*(2), 209-228.

[57] Chopp, D. L. (1993). Computing minimal surfaces via level set curvature flow. *Journal of Computational Physics*, *106*(1), 77-91.

[58] Peng, D., Merriman, B., Osher, S., Zhao, H., & Kang, M. (1999). A PDE-based fast local level set method. *Journal of computational physics*, *155*(2), 410-438.

[59] Zhang, K., Zhang, L., Song, H., & Zhou, W. (2010). Active contours with selective local or global segmentation: a new formulation and level set method. *Image and Vision computing*, *28*(4), 668-676.

[60] Talu, M. F. (2013). ORACM: Online region-based active contour model. *Expert Systems with Applications*, *40*(16), 6233-6240.

[61] Altarawneh, N. M., Luo, S., Regan, B., Sun, C., & Jia, F. (2014). Global threshold and region-based active contour model for accurate image segmentation. *Signal & Image Processing*, *5*(3), 1.

[62] Akram, F., Kim, J. H., Lim, H. U., & Choi, K. N. (2014). Segmentation of intensity inhomogeneous brain MR images using active contours. *Computational and mathematical methods in medicine*, *2014*.

[63] Yang, Y., & Wu, B. (2012). Convex image segmentation model based on local and global intensity fitting energy and split Bregman method. *Journal of Applied Mathematics*, *2012*.

[64] Zhang, K., Zhang, L., Lam, K. M., & Zhang, D. (2013). A local active contour model for image segmentation with intensity inhomogeneity. *arXiv preprint arXiv:1305.7053*.

[65] Ojala, T., Pietikainen, M., & Maenpaa, T. (2002). Multiresolution gray-scale and rotation invariant texture classification with local binary patterns. *IEEE Transactions on pattern analysis and machine intelligence*, *24*(7), 971-987.

[66] Mäenpää, T. (2003). *The local binary pattern approach to texture analysis: extensions and applications*. PhD thesis, Acta Universitatis Ouluensis C 187, University of Oulu.

[67] Teutsch, M., & Beyerer, J. (2012, November). Noise resistant gradient calculation and edge detection using local binary patterns. In *Asian Conference on Computer Vision* (pp. 1-14). Springer Berlin Heidelberg.

[68] Ahonen, T., Hadid, A., & Pietikainen, M. (2006). Face description with local binary patterns: Application to face recognition. *IEEE transactions on pattern analysis and machine intelligence*, *28*(12), 2037-2041.

[69] Mandava, A. K., & Regentova, E. E. (2012). Speckle Noise Reduction Using Local Binary Pattern. *Procedia Technology*, *6*, 574-581.

[70] Teutsch, M., Trantelle, P., & Beyerer, J. (2013, September). Adaptive real-time image smoothing using local binary patterns and Gaussian filters. In *2013 IEEE International Conference on Image Processing* (pp. 1120-1124). IEEE.

[71] Mukherjee, S., & Acton, S. T. (2015). Region based segmentation in presence of intensity inhomogeneity using legendre polynomials. *IEEE Signal Processing Letters*, *22*(3), 298-302.